Multidisciplinary Study of Soft Shape Morphing Systems

by

Mohammad Ali Kazemi Lari

A dissertation submitted in partial fulfillment
of the requirements for the degree of
Doctor of Philosophy
(Aerospace Engineering)
in The University of Michigan
2021

Doctoral Committee:

Professor John Shaw, Chair
Professor Daniel Inman
Professor Anthony Waas
Professor Alan Wineman

Mohammad Kazemi

mkazemi@umich.edu

ORCID iD: 0000-0003-3964-5933

DEDICATION

To my family.

ACKNOWLEDGEMENTS

This research was supported by the U.S. National Institutes of Health (R01 HL123526, R01 HL141460, and R01 HL 149431) and the University of Michigan Rackham Graduate School (Rackham Graduate Student Research Grant and Rackham Conference Travel Grants).

I am tremendously grateful to everyone who supported me during my graduate studies. Many thanks especially to my advisor, Dr. John Shaw, for giving my the opportunity to learn from him, for his unwavering support, thoughtful guidance, and caring patience.

Many additional thanks to my collaborators including Dr. Alan Wineman, Dr. Ye Chen-Izu, and Dr. Leighton Izu who have made this research possible.

Special thanks to my committee members: Dr. Daniel Inman, Dr. Anthony Waas, and Dr. Alan Wineman for providing their expert insight and opinion.

I would also like to thank the many students and researchers from whom I learned so much, especially to previous members of the Adaptive Materials and Structures Laboratory including Daniel Biggs, William Lepage, and Corin Bowen for all of their help, advice, and thought-provoking conversations.

Thank you to all the University of Michigan Aerospace Engineering Department staff who shared their suggestions, critiques, equipment, and expertise, including Thomas Griffin, David Mclean, Aaron Borgman, Terry Larrow, and Christopher Chartier, among many others.

Thank you to all my friends for always being there for me and making so many ordinary moments, extraordinary.

Thank you to my amazing sister Zeinab and my brother in-law Mehdi for bringing smile on my face and always being encouraging and supportive.

Thank you immensely to my parents Mohammad Reza and Maryam for their unconditional love and for fostering curiosity and making so many sacrifices for my education and growth.

Finally, I am most grateful to my wonderful wife Delaram, for your steadfast love, for standing by my side for every step of this journey, and for believing in me. Thank you for making my life abundantly joyful.

TABLE OF CONTENTS

LIST OF FIGURES

Figure

LIST OF TABLES

Table

ABSTRACT

Nature abounds with examples of shape morphing systems where an entity either gradually grows into a complex 3-D shape pattern or rapidly morphs into a new configuration. Inspired by the shape shifting capabilities of biological systems, in this work we study the response of natural and synthetic morphing systems through a few examples. These include the *in vitro* adaptive contraction of a cardiac muscle cell inside a constraining hydrogel, inflation of architectured rubber membranes, and a shape morphing soft robot.

Cardiac muscle cells (cardiomyocytes), have an intrinsic mechano-chemo-transduction (MCT) mechanism that enable them to automatically convert mechanical loads into biochemical signals to actively regulate their amplitude and speed of contraction. At the molecular level, this is attributed to the morphing of regulatory and motor proteins (actin and myosin filaments) to facilitate muscle contraction. The underlying MCT mechanisms, however, are unclear and currently under investigation. To help decipher these mechanisms, we develop a mathematical model, as a companion tool for the experimental *in vitro* Cell-in-Gel system of our collaborators, to analyze the time-dependent, 3-D strains and stresses within a cardiomyocyte contracting in a viscoelastic medium. The model utilizes the exact analytical solution of the viscoelastic Eshelby inclusion boundary value problem as an efficient computational tool to simulate the mechanical fields inside and outside the cardiomyocyte.

In a second study, we investigate the inflation of shape morphing synthetic soft composites with architectured geometry and material properties. Such shape morphing systems could have desirable applications in space deployable systems where there is a growing demand for energy-efficient lightweight and low-cost structures. These structures possess an exceptionally high mechanical packaging efficiency and very small stowage volume, which makes them attractive candidates for space applications including antenna reflectors, solar arrays, inflatable rovers, re-entry equipment, and human habitats. In particular, we explore several feasible 3-D shapes that can be achieved through the inflation of an initially flat rubber membrane with nonuniform geometrical and material properties. Our rubber-based prototypes provide a convenient basis for conceptual scientific and design explorations in shape morphing inflatable structures.

In a third study, we explore the idea of shape shifting in the design and fabrication of synthetic soft robots with active components. Motivated by the swimming mechanisms of

jellyfish, we develop a novel concept for a soft biomimetic underwater robot that imitates the shape and kinematics of the typical animal. The robot swims by harnessing the buckling instability of its soft body to quickly morph from an initially flat into a deformed dome-shaped configuration, which generates the required thrust for underwater locomotion. Joule heating of an embedded pre-stretched shape memory alloy spring, serves as an artificial muscle for the robot to make this shape morphing possible. The proposed synthetic shape morphing system introduces a new idea in design of simple, compact, and biomimetic robots with smart artificial muscles.

CHAPTER 1

Introduction

1.1 Shape morphing systems

Shape morphing systems are those that are capable of changing their shapes from an initially stable configuration into other (usually stable) configurations in response to external stimuli or change in the environmental conditions. Nature abounds with biological systems that morph their shapes in order to reach to a configuration that enables a special functionality. The most tangible examples of such natural shape-changing mechanisms are the morphogenetic processes in botany, usually observed in plant leaves (Figure 1.1) as they grow over the early stages of their life-span [1, 2, 3]. These changes usually happen very slowly, on the order of days or months.

Other types of shape-changes in plants generally happens as the movement of one organ in relation to the whole plant. These categories of morphing are quite widespread in occurrence and are known to be related to a single physiological process, the change in volume of special motor cells. One fundamentally important example of such particular shape-changes, is the opening and closing of stomata, which provides a basic control of photosynthesis and is often much quicker than the morphogenetic processes, usually on a time scale of minutes [4].

Shape morphing in plants can also occur rapidly (on a time scale of milliseconds), such as the snap of the insectivorous trap of Dionaea (Venus flytrap), the pollination movement of the Stylidium (trigger plant) [6, 4, 7], or the thigmonastic movements in the sensitive plant Mimosa pudica [8]. These rapid shape-changes, happen as a result of external stimuli, generally in the form of an externally applied physical force, electrical potential, heat, etc. Moreover, shape morphing in natural systems are either reversible such that the original shape and configuration can be recovered after the shape-change or irreversible such that the change in shape is permanent and irrecoverable. The morphogenesis growth of plant leaves is an example of irreversible shape-shifting processes while the snap of Dionaea's trap is a reversible shape-change.

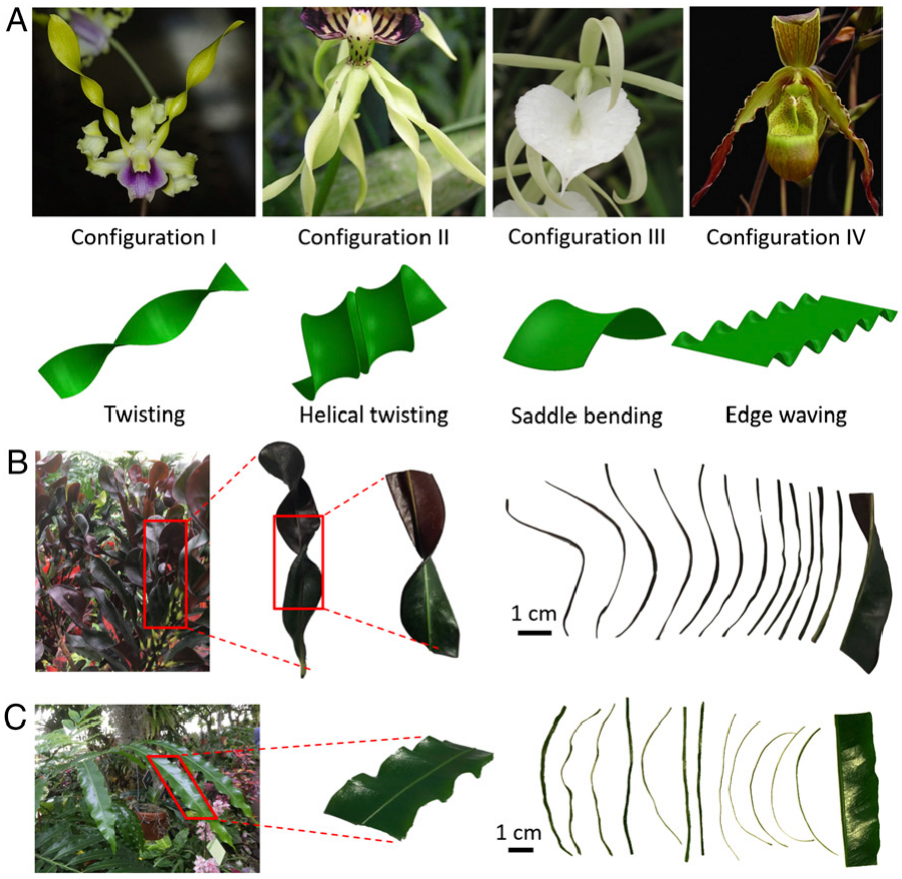

Figure 1.1: Morphogenetic processes in botany, from [2]. (A) 3D morphologies of orchid petals with their corresponding buckling configurations, (B) twisting croton mammy (codiaeum variegatum) leaf and, (C) edge-waving fern tree (filicium decipiens) leaf.

Shape morphing is also observed in animals. An outstanding example is the recently discovered frog species, known as the "Punk Rocker" frog (scientifically named Pristimantis mutabilis) which is capable of shifting its skin shape from smooth to a textured (spiny) configuration in under six minutes [9]. It is believed that its thorn-like spine helps the animal to camouflage into its mossy surrounding, by changing its skin shape, a process that has not been observed in any other vertebrate.

Also, it is commonly observed that birds actively morph the shape of their wings during flight in order to control and stabilize their flight paths [10]. In addition, a common practice among birds is the span-wise bending of the wing tip feathers (Figure 1.4) in order to enhance the efficiency of flight through reduction of the drag forces [11]. They achieve their morphing capability by incorporating flexible lifting surfaces that are actuated through structural elements connected to their wing muscles.

Despite the anatomical and structural differences, the cellular level difference are responsible for the differences in shape morphing between plants and animals. In animals,

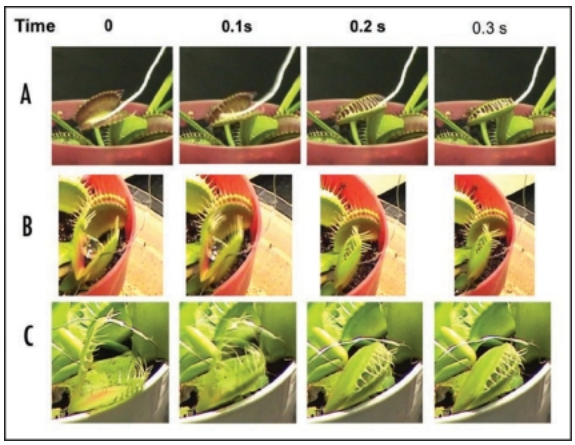

Figure 1.2: Closing of Venus flytrap in response to stimuli. (A) Effect of mechanical stimulation by a cotton thread, (B) feeding by gelatin, and (C) and by electrical 14 μC stimulus. From [5].

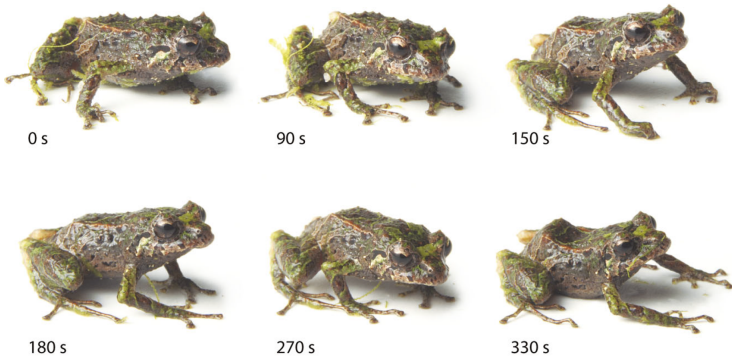

Figure 1.3: Time frames of skin texture variation in one individual frog (Pristimantis mutabilis) from Reserva Las Gralarias (Pichincha, Ecuador). From [9].

shape morphing depends primarily on the action of cellular contractile proteins which rely on mechano-chemo-transduction (MCT) mechanisms to transduce biochemical into mechanical energy. This is possible because unlike plant cells and tissues, most animal tissues are soft and can be easily morphed into a different shape. Plants are built from vacuolated cells surrounded by walls which are usually relatively rigid. This makes it highly unlikely that contractile proteins can function to generate concerted movement in a similar way to that in animals [4]. Plants do have contractile systems but they operate based on intracellular mechanisms like cytoplasmic streaming and chromosomal movement [4]. To achieve movement, plants use a change in hydrostatic or turgor pressure in special motor cells which leads to a change in volume and length; and it is the latter which produces the required displacement [4].

Shape morphing is also observed at cellular level. Cardiac and skeletal muscle cells (myocytes) are magnificent examples of biological structures that are capable of actively

Figure 1.4: Different morphologies of wingtip feathers in birds. (A) Kea. (B) Pacific Brown Pelican. (C) Red Tailed Hawk. (D) Bald Eagle. (E) Northern Hawk Owl. (F) Great Blue Heron. The slotted configuration of wingtip feathers is thought to reduce the lift-induced drag caused by wingtip vortices. From [12].

deforming their originally relaxed shapes into a contracted configuration in response to biochemical signals. Within each myocyte are long filaments known as myofibrils which are in turn composed of smaller units known as sarcomeres Figure 1.5. A sarcomere is the functional unit of cardiac and skeletal muscle cells and these are arranged end-to-end, creating a long chain of contractile "springs in series". A parallel array of sarcomeres contracting in unison are able to initiate a large force in the muscle.

Contraction of sarcomeres is essentially achieved through the interplay of two types of myofilaments inside each sarcomere: thick filaments composed primarily of the contractile myosin protein and thin filaments, composed primarily of the contractile actin protein. Hundreds of thin filaments of actin are attached to the capping Z-disc at each end of the sarcomere, and thick filaments of myosin, cross-linked at the center by the M-line, are interdigitated with the actin filaments. The straited pattern observed by microscopy, results from the overlapping (anisotropic) and non-overlapping (isotropic) regions of actin and myosin. It is the cross-bridging of these two filaments that is responsible for the sarcomere's contraction. In particular, the myocin head and tropomyosin, which is a helically coiled protein around the actin myofilament, morph their shapes to allow myosin head to anchor to the actin filament and initiate the contraction (Figure 1.6), analogous to a ratchet and pawl mechanism. Myocytes can also regulate the extent of their contractility in response increased load on

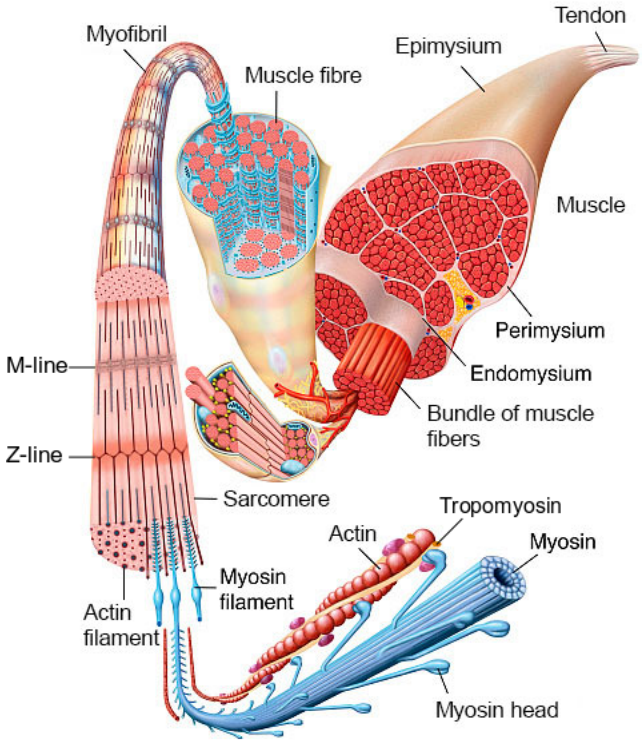

Figure 1.5: The hierarchical structure of a skeletal muscle, an active contracting system. Inside, each muscle fiber is composed of myofibrils, which are in turn composed of sarcomeres, the individual units of contraction. Motion is achieved by the grasping of actin by myosin, which draws the filaments together. Reproduced from [13].

them. This is achieved using hierarchical principles, triggered when the released calcium ions (Ca^{2+}) into the cytosol, diffuse into and bind to the myofilament proteins which results in macroscale contraction from staggered fibrous structures. This process is defined as the excitation–contraction coupling (ECC) which describes the rapid communication between electrical events occurring in the plasma membrane of the muscle fibres and Ca^{2+} release from the sarcoplasmic reticulum (SR), which leads to contraction [14].

As demonstrated in Figure 1.6, the myosin heads at both ends of the thick filament bind to the open sites on the actin filaments and generate a power stroke in a process called the cross-bridge cycle following the sliding filament theory of striated muscle contraction. In a sense, the myosin heads 'walk' along the actin filament, producing sliding of the actin and myosin filaments and sarcomere shortening. Cross-bridge cycling occurs in the presence of Ca^{2+} and uses adenosine triphosphate (ATP) as an energy source [16]. In skeletal muscles the reduction in the distance between Z-units, and thus the length of the sarcomeres, can be around 70% [17]. Contraction of the sarcomeres adds together in series to produce a cell contraction magnitude that is nearly proportional to the change in sarcomere length. Muscle

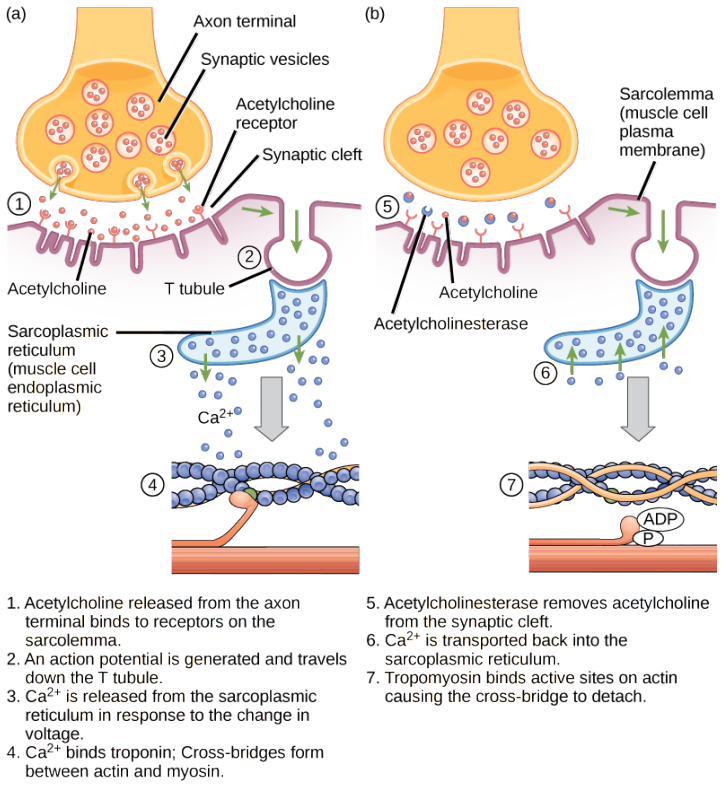

Figure 1.6: The excitation–contraction coupling in a skeletal muscle contraction. The myocin head and tropomyosin (the helically coiled protein around actin) morph their shapes to allow myosin head to anchor to the actin filament, [15].

fibers are then bundled into muscle fascicle, which define the direction of contraction of the muscle tissue and enable the complex motions enabled by muscles [17]. These range from the 486 m s^{-2} acceleration achieved by the chameleons tongue to the exquisite shape control of cuttlefish papillae [17, 18, 19]. The degree of macroscale muscle contraction varies between approximately 20–40% [17, 20].

Analogous to biological systems, synthetic architectured composites can adapt and regulate their response and performance to the change in environmental conditions or external stimuli, simulating, in this way, the behavior of natures materials. These systems can be designed to meet specific requirements and adapt to the needs of users through tailored properties which can be either composed of passive components or active components (usually through "smart" materials) or a combination of both. The shape deformation capability, as an intrinsic material characteristic of adaptive materials (shape memory alloys, shape memory polymers electrostrictive, magnetostrictive, photostrictive, ...), offers a great advantage as it allows small component dimensions in comparison to conventional systems and enables to perform a task at a lower energy use, emission, harm to the ecosystem, and smaller size (higher energy-density). These materials have the characteristic to detect an external stim-

ulus and to initiate appropriate action by adapting their material properties. The creation of synthetic systems that can morph in a controlled manner, as seen in nature, has recently driven advances in many fields of fundamental and applied sciences.

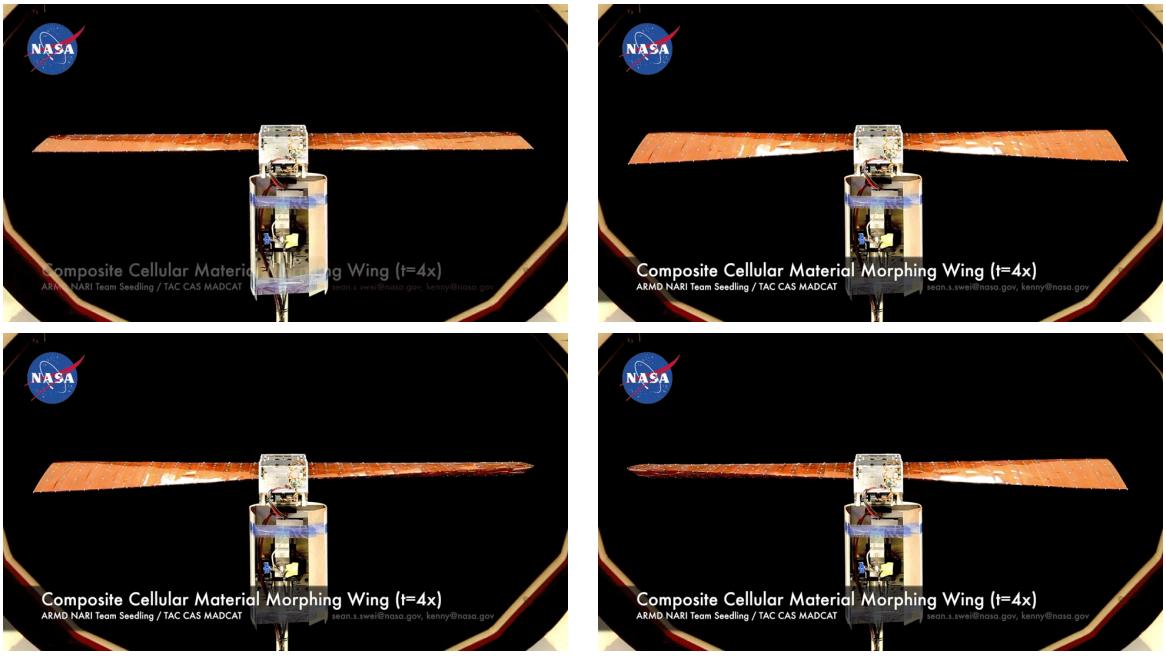

Figure 1.7: Selected time frames of a composite morphing wing design idea developed by NASA. The wing is constructed from building-block units made of advanced carbon fiber composite materials. Reproduced from [21].

The tremendous interest in self-shaping materials stems from a wide range of applications for these materials, ranging from biomedical devices to aircraft design [22, 23, 6]. A morphing aircraft wing is a great example of a synthetic shape morphing system that allows tuning the span-wise shape of the wing based of the aerodynamic needs at a specific speed or maneuver. A prototype example of a morphing wing idea developed by NASA is shown in Figure 1.7. The wing is constructed from building-block units made of advanced carbon fiber composite materials. These building blocks are assembled into a lattice, or arrangement of periodic structures [24]; the way that they are arranged determines how they flex. The wing also features actuators and computers that make it morph and twist to achieve the desired wing shape during flight. This concept allows having a wing that is more efficient, as a rigid wing with a limited number of moveable surfaces is only a compromise and can not be the most efficient shape of any given flight phase. Such an efficient morphing design would yield a better fuel economy which would in turn reduce the overall weight of the aircraft.

Shape memory alloys (SMAs), as a family of smart and adaptive materials, have also been explored in shape morphing structures. A well-employed application of such active shape

morphing systems is found in the design and fabrication of reconfigurable composite chevrons that are effective for noise reduction at the exhaust of jet engines. Figure 1.8 demonstrates Boeing's design for a morphing chevrons that uses SMA beams as active elements for shape shifting.

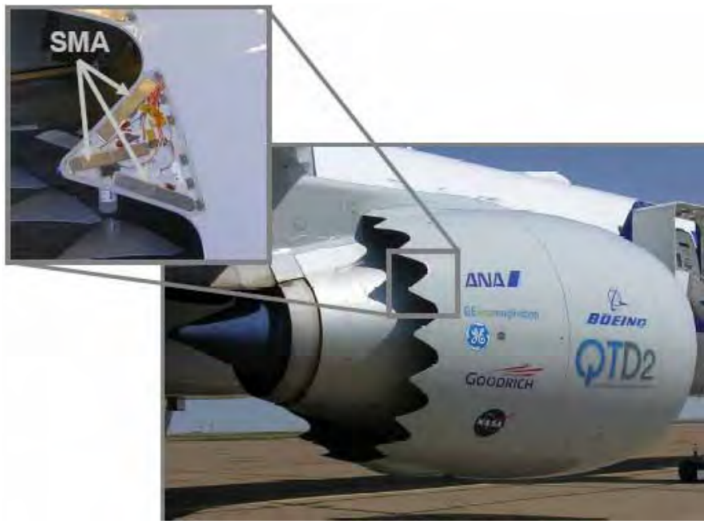

Figure 1.8: Boeing's morphing geometry chevron actuated using SMA beams. From [25], originally reproduced from [26].

Soft materials like elastomers and hydrogels are also desirable structural components for the design of synthetic shape morphing structures. They enjoy unique characteristics, including biocompatibility, adaptability, multifunctionality, low cost, and tunable stiffness and strength [27, 28] and are promising components for synthesizing new materials that can acquire a pre-programmed shape in response to stimuli [29, 6]. Soft materials can be tailored to induce simple bending, twisting and wrinkling motions through modulation of structural elements [30, 31, 32] or can be programmed to attain a complex 3D shapes in response to stimuli [33, 34, 35, 36, 37]. Such soft synthetic shape reconfigurable structures can find applications in drug delivery [38], tissue engineering [39], actuators [40], and soft robotics [41]. An example of a mesostructured elastomer plate that undergoes a fast, controllable and complex shape transformations under applied pressure is demonstrated in Figure 1.9. The geometric restrictions are overcome by precisely controlling the local growth rate and direction through a specific network of airways embedded inside the rubber plate.

1.2 Overview

Inspired by the shape shifting capabilities of biological systems, in this work, the response of natural and synthetic morphing systems are studied through a few examples.

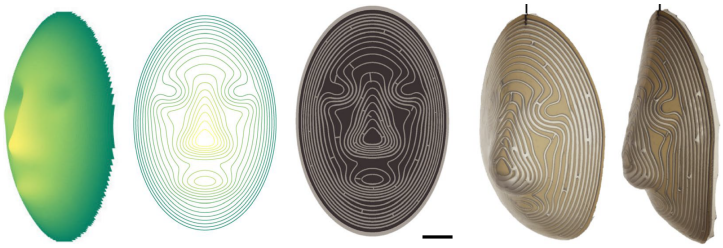

Figure 1.9: Shape programming of a pneumatic shape-morphing elastomeric face, reproduced from [37]. From left to right: the target shape, the corresponding deformation contour lines, the network of channels computed to give rise to the target metrics, and two pictures of the morphed geometry.

These include the *in vitro* adaptive contraction of a cardiac muscle cell inside a constraining hydrogel, inflation of architectured rubber membranes with nonuniform geometrical and material properties, and a shape morphing soft underwater robot.

Chapter 2 focuses on an example of natural shape morphing systems, contraction of heart muscle cells, and aims to attain a better understanding of the mechanisms through which each cardiac muscle cell (cardiomyocyte) regulates its amplitude and speed of contraction. We develop a mathematical viscoelastic Eshelby inclusion model, as an efficient computational companion tool for the *in vitro* Cell-in-Gel system of our collaborators, to analyze the time-dependent, three-dimensional (3D) strains and stresses within a cardiomyocyte contracting in a viscoelastic medium. A new mathematical feedback framework is demonstrated to account for the mechano-chemo-transduction (MCT) mechanism that captures the load-adaptive autoregulatory response of the cell. This work provides important clues to uncovering the cellular and molecular mechanisms that underlie the autoregulation pathways that adjust the force and contractility of cardiomyocytes in healthy hearts. Part of the findings of this chapter has been published in [42], and the most recent results are now under review in a peer-reviewed journal.

Chapter 3 investigates the shape morphing ability of architectured soft composites with passive components. In particular, several feasible 3D shapes that can be achieved via inflation of an initially flat circular rubber membrane with nonuniform geometrical and material properties, are explored. Design, fabrication, and testing of these membranes are presented in this chapter and finite-element simulations are accompanied to perform a study on the design parameters. Our rubber-based prototypes provide a convenient basis for conceptual scientific and design explorations of shape morphing inflatable structures.

Chapter 4 explores an application of compliant shape morphing systems in the framework of a synthetic soft underwater robot. A novel concept in the design of a robotic jellyfish that imitates the shape and kinematics of the typical animal is demonstrated. The robot

swims by harnessing the buckling instability of its soft body to morph from an initially flat configuration into a deformed shape which generates the required thrust for underwater locomotion. The main contribution of this work is the simplicity of design, requiring only a soft rubber matrix with a single embedded SMA spring acting as the artificial muscle. The results and findings of this chapter have been published in [43, 44]

Finally, conclusions and future work are summarized in Chapter 5.

CHAPTER 2

Analysis of Cardiac Myocyte Contraction in a 3D Viscoelastic Medium

2.1 Introduction

The heart is a remarkably "smart" pump. During each heartbeat, cardiac muscle cells in the left ventricle generate contractile forces to pump blood against systemic vascular resistance, while maintaining adequate cardiac output in the presence of blood pressure changes that accompany our various daily activities (e.g. posture change and exercise). The heart's intrinsic ability to adapt to changing mechanical loads is manifested in the Frank-Starling and Anrep effects, first reported over a century ago [45, 46, 47]. The cellular and molecular origins of the heart's autoregulation, however, remain incompletely understood [48, 49, 50, 51]. Studies suggest that cardiomyocytes have intrinsic mechano-chemo-transduction (MCT) mechanisms that sense and transduce mechanical loads into biochemical signals to regulate the contractile force [51, 52, 53]. Multiple MCT pathways have been hypothesized in an effort to clearly identify the mechano-sensors and chemo-transducers that regulate the Ca^{2+} signaling system and contractility [54]. These pathways appear to provide closed-loop feedback between the mechanical loading and the excitation-Ca^{2+} signaling-contraction coupling, which enables the cardiomyocyte to autoregulate contractility in compensatory response to varying physiological loads. Such MCT pathways may be diminished or absent in certain diseases, and even in healthy hearts, excessive load can cause Ca^{2+} dysregulation and contractile dysfunction that lead to cardiac arrhythmias and heart failure. The mechanical stress levels that cause such failure in cardiomyocytes, however, have never been quantified.

To help decipher the MCT mechanisms at the single-cell level, we developed the Cell-in-Gel system in which freshly isolated live cardiomyocytes are embedded in a constraining hydrogel and then stimulated to undergo excitation-Ca^{2+} signaling-contraction [55]. The hydrogel is a 3-D polymer matrix immersed in a physiological solution *in vitro* that mimics

the extracellular matrix by providing a viscoelastic medium to impose mechanical resistance during cardiomyocyte contraction. In physiological (healthy) conditions, the cardiomyocyte contracts and relaxes in synchrony with surrounding cells to pump blood in the presence of chamber pressure. In pathological conditions, such as infarction, fibrosis, arrhythmias and asynchronous contraction, the cardiomyocyte may contract asynchronously against its neighbors and experience more severe multiaxial mechanical stresses. While it is extremely difficult to mimic the exact *in vivo* conditions, the Cell-in-Gel system enables us to study the impact of mechanical stresses on a single cardiomyocyte in a controlled way [55]. To simulate the normal or overload in healthy or diseased states, hydrogels of various viscoelastic moduli are used to systematically vary the afterload during cardiomyocyte contraction in the Cell-in-Gel experiments. Although the mechanical strains during cell contractions can be measured by optical microscopy, the mechanical stresses in the cell cannot be directly measured and must be inferred by analysis.

Herein, a mathematical model to quantify all mechanical fields is presented, as a companion tool to help guide ongoing Cell-in-Gel experiments and to interpret the experimental data. The model is based on the classical Eshelby problem of an ellipsoidal inclusion embedded in an elastic matrix, which has a known analytical solution [56, 57]. We used this previously to analyze Cell-in-Gel experiments by treating the gel as a purely elastic (non-viscous) matrix and the cell as an elastic inclusion that undergoes an eigenstrain (spontaneous inelastic strain) to simulate contraction [58]. To improve the fidelity of the analysis, the previous model is extended in this work to account for two important features:

(1) viscoelastic properties of the hydrogel and the cardiomyocyte,

(2) the cardiomyocyte's autoregulation in response to changes in mechanical afterload.

To address item (1), the *viscoelastic* solution of the Eshelby inclusion problem is applied to the Cell-in-Gel system. The Correspondence Principle of Linear Viscoelasticity was first used to extend the Eshelby solution in [59], although used for a very different purpose (to estimate the effective mechanical properties of synthetic particulate composites). We use a similar approach, but rather than employ the eigenstrain concept as a mathematical artifice to seek a homogenized solution to a heterogeneous composite, we seek the explicit mechanical fields to a biomechanics problem. Importantly, the eigenstrain of the inclusion here has a physical interpretation as muscle cell contractility.

To address item (2), we propose a mathematical feedback model to capture the up-regulation in cytosolic Ca^{2+} transients in response to elevated mechanical stress in the cell. The increased Ca^{2+} in turn, leads to enhanced cell contractility in the mathematical form

of an amplified eigenstrain (contractility). The viscoelastic Eshelby solution takes the time-dependent eigenstrain as the input and calculates the cell's stress as the output to complete the feedback loop. Differential equations are proposed in the feedback model, and these are calibrated to a few Cell-in-Gel experimental measurements for the first time. We believe this framework is novel, and it can be easily adapted and refined as more extensive data sets become available from ongoing Cell-in-Gel experiments. Our ultimate aim, by developing an accurate mechanical analysis of the 3-D stresses in the cardiomyocyte, is to establish a mathematical and physical foundation to better understand how the cell senses multi-axial stresses, activates mechano-sensors at various locations, transduces those stresses to biochemical signals, and autoregulates contractile force in adaptive response to load changes.

This paper begins with an overview of the Cell-in-Gel experiments in Section 2.2, followed by a brief review of linear viscoelasticity theory and the mechanical characterization of both gel and cell materials in Section 4.2.2. In Section 4.3, the boundary value problem is defined in the context of the elastic Eshelby inclusion problem. Its analytical solution is leveraged to solve the corresponding viscoelastic problem by exploiting the Correspondence Principle of Viscoelasticity and a Discrete Fourier Transform (DFT) analysis to enable fast computations of periodic time-dependent mechanical fields. Section 2.5 provides an example simulation of a baseline case, followed by a parameter study to investigate the influence of material properties and cell geometry. Each simulation predicts the interior (cell) and exterior (hydrogel) displacement fields that can be compared to experimental measurements. The model is used to calculate the multiaxial stress state inside the cell (affecting internal mechano-sensors), the traction distribution on the cell surface (affecting surface mechano-sensors), and the mechanical work and power generated by the cell (related to metabolic expenditure). The mechanical analysis is then embedded in a proposed feedback control framework, which links the stress-dependent Ca^{2+} transients to the cell's adaptive contractile response. Finally, a summary and conclusions are provided in Section 2.6.

2.2 The Cell-in-Gel system

The Cell-in-Gel system was developed by us as an experimental tool (see Figure 2.1) to apply controlled 3-D mechanical loading on a single cardiomyocyte to enable an in-depth investigation at the cellular and molecular levels. Ventricular myocytes (Figure 2.1A) were freshly isolated from a healthy rabbit heart [60] and loaded with the fluorescent Ca^{2+} indicator Fura-2 [55]. The cells were then embedded in the hydrogel and continuously perfused with Tyrodes solution (Figure 2.1B). The hydrogel consisted of polyvinyl alcohol (PVA) and polyethylene glycol (PEG)-boronate cross-linked polymer matrix immersed in an aqueous

solution. It provided a soft and viscous medium, against which the contracting cell encountered mechanical resistance. The boronate-base crosslinker also binds to the glycosylated molecules on the cell surface to attach the cell to the polymer matrix. As the cell contracted and relaxed, the hydrogel deformation could also be tracked via confocal microscopy by the motion of embedded microbeads.

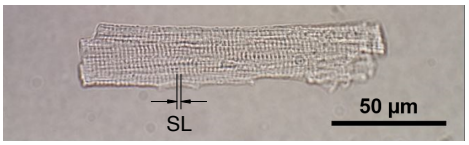

A. Rabbit left ventricular myocyte

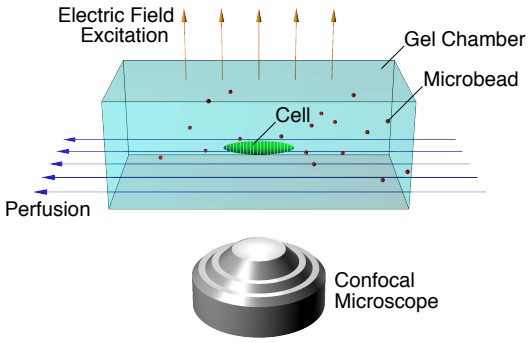

B. Schematic of setup

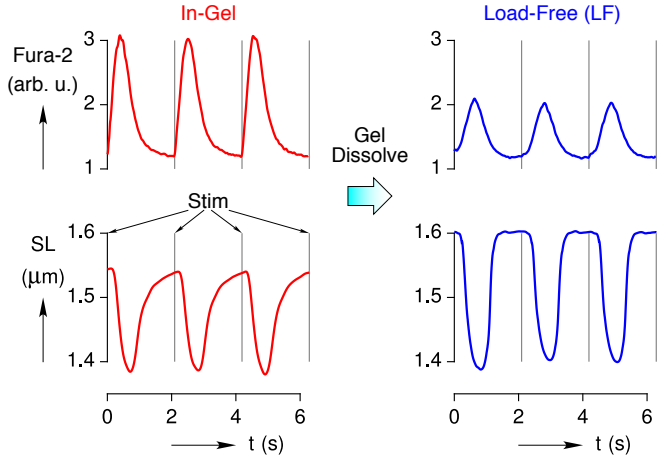

C. Cytosolic Ca^{2+} (Fura-2) and sarcomere length (SL) histories

Figure 2.1: The Cell-in-Gel system and typical results.

The in-gel cardiomyocyte was paced at approximately 0.5 Hz frequency using electric field excitation pulses (suprathreshold, 4 ms) to undergo excitation-Ca^{2+} signaling-contraction cycles. As depicted in Figure 2.1C, intracellular cytosolic Ca^{2+} transients ($\left[Ca^{2+}\right]_i$, shown

in upper panel) and cell contractions (shortening of sarcomere length, shown in lower panel) were measured simultaneously using epi-fluorescence microscopy. Measurements on a single cardiomyocyte were first performed when the cell was contracting in-gel under mechanical load (left panel). The gel was then dissolved to release the cell inside the solution, and contraction of the same cell was measured again under load-free conditions (right panel) [**?**]. Such self-control experiments clearly showed that the cardiomyocyte had significantly larger Ca^{2+} transients under mechanical load than when load-free. Hence, the mechanical load exerted by the surrounding hydrogel was sensed by the cell and transduced to biochemical signal to upregulate the Ca^{2+} transients. This MCT mechanism led to a MCT-Ca^{2+} gain that enhanced the contractility of the cardiomyocyte in response to increased load. (It will be shown in Section 2.5 that a smaller change in SL would have occurred without this gain.)

In the classical paradigm of cardiac excitation-contraction coupling, the action potential causes the Ca^{2+} transient which in turn results in muscle contraction. Previous mechanistic studies mostly focused on the forward action from the electrical system to the Ca^{2+} signaling system, and then to the contractile system. The Cell-in-Gel method enables one to control the afterload on a single cardiomyocyte and provides new information on how mechanical load feedback affects the Ca^{2+} signaling system. Consistent with control theory, such closed-loop feedback enables autoregulation of contractility in response to load changes. For more than a century it is known that the heart has the remarkable ability to autoregulate contractility to compensate for mechanical load changes in order to maintain constant cardiac output. However, the molecular structures responsible for the autoregulation observed at the heart and tissue level remain unclear. The Cell-in-Gel technique provides a modern tool for in-depth investigation of MCT mechanisms at the single cell, sarcomere, and molecular levels. Ongoing Cell-in-Gel experiments, which will be reported elsewhere in experimental papers, have generated extensive structural and functional data to probe the origins of MCT mechanisms. The main focus of this modeling paper is to illustrate how a precise 3-D mechanical analysis of the strain and stress fields of the cardiomyocyte in a viscoelastic environment can be determined, thereby interpreting the experimental data, in order to better understand the MCT mechanisms in a quantitative way.

2.3 Materials characterization

The mechanical analysis of Section 4.3 requires that the constitutive behaviors of the hydrogel and the cardiomyocycte be known. Both are treated here as viscoelastic materials. Our hydrogel consists of three main constituents: PVA, PEG-boronate cross-linker, and physiological solution (e.g. Tyrodes or phosphate-buffered saline). Each of these components

has a considerable effect on the viscoelastic properties of the hydrogel, so the magnitude of the applied mechanical load can be fine-tuned by adjusting the concentrations of these constituents. Hydrogels of various cross-link densities are used in the Cell-in-Gel experiments to systematically vary the mechanical resistance to cardiomyocyte contraction. This section provides a brief review of linear viscoelasticity theory, followed by the mechanical characterizations of the hydrogel and the cardiomyocyte.

2.3.1 Linear viscoelasticity

According to the theory of linear viscoelasticity, the constitutive (stress-strain) response of the material can be expressed as a convolution integral in terms of a relaxation modulus and a prescribed strain history. That is, for a given shear strain history $\gamma(t)$, the shear stress $\tau(t)$ history is expressed in terms of the relaxation shear modulus $G(t)$ as

$$\tau(t) = G(t)\,\gamma(0^+) + \int_{0^+}^{t} G(t-s)\dot{\gamma}(s)\,\mathrm{d}s, \tag{2.1}$$

where $\dot{\gamma} = \mathrm{d}\gamma/\mathrm{d}t$ is the strain rate. If the strain input is a step function at time $t = 0$ according

$$\gamma(t) = \begin{cases} 0, & t < 0 \\ \gamma_0, & t \geq 0 \end{cases} \tag{2.2}$$

where γ_0 is a constant, the response is simply $\tau(t) = \gamma_0 G(t)$. Thus, the relaxation modulus $G(t) = \tau(t)/\gamma_0$ is the stress response to a unit step strain input. For a typical viscoelastic solid the stress jumps to an initial value G_0 at time $t = 0^+$ and then decays monotonically as $t \to \infty$ to a smaller positive value G_∞.

To capture the viscoelastic behavior of real hydrogels from rheology data with reasonable accuracy, the relaxation modulus $G(t)$ is approximated here by a generalized Maxwell viscoelastic model, consisting of a spring of stiffness G_∞ assembled in parallel with multiple Maxwell elements. The relaxation modulus is then mathematically represented by a Prony series according to [61]

$$G(t) = G_\infty + \Delta G \sum_{j=1}^{N_\tau} \xi_j\, e^{-t/\tau_j}, \tag{2.3}$$

where G_∞ is the asymptotic value as $t \to \infty$, $\Delta G = G_0 - G_\infty$, τ_j $(j = 1, 2, \ldots, N_\tau)$ are relaxation time constants (not to be confused with the shear stress), and ξ_j represent 'phase

fractions' that apportion the amount of material that relaxes according to each time constant τ_j. To ensure it is physically reasonable and to preserve the interpretation of G_0 and G_∞ as instantaneous short-term and long-term values, respectively, the fractions must be non-negative $\xi_j \geq 0$ (for all $j = 1, 2, \ldots, N_\tau$) and satisfy $\sum_{j=1}^{N_\tau} \xi_j = 1$.

If strain input is oscillatory, say $\gamma(t) = \gamma_0 \sin \omega t$ where ω is a prescribed angular frequency, the resulting shear stress history, $\tau(t)$ by Equation (2.1), is

$$\frac{\tau(t)}{\gamma_0} = G' \sin \omega t + G'' \cos \omega t - \Delta G \sum_{j=1}^{N_\tau} \frac{\omega \tau_j \xi_j}{1 + \omega^2 \tau_j^2} e^{-t/\tau_j}, \tag{2.4a}$$

$$G' = G_\infty + \Delta G \sum_{j=1}^{N_\tau} \frac{\omega^2 \tau_j^2 \xi_j}{1 + \omega^2 \tau_j^2}, \tag{2.4b}$$

$$G'' = \Delta G \sum_{j=1}^{N_\tau} \frac{\omega \tau_j \xi_j}{1 + \omega^2 \tau_j^2}. \tag{2.4c}$$

After a sufficiently long time the decaying part in Equation (2.4a) can be neglected, leaving the steady oscillatory response

$$\frac{\tau(t)}{\gamma_0} = G' \sin \omega t + G'' \cos \omega t. \tag{2.5}$$

The quantity that characterizes the in-phase portion of the response G' is called the *storage modulus*, while that for the out-of-phase portion G'' is called the *loss modulus*. These are frequency-dependent functions which can be measured in a modern dynamical mechanical analyzer. To see the phase δ explicitly, one can rewrite Equation (2.5) as $\tau(t)/\gamma_0 = |G| \sin(\omega t + \delta)$, where $\tan \delta = G''/G'$ and $|G| = \sqrt{(G')^2 + (G'')^2}$.

Alternatively, using complex variables[1], suppose the input strain history is oscillatory according to $\widehat{\gamma}(t) = \gamma_0 e^{i\omega t} = \cos \omega t + i \sin \omega t$ (by Euler's relation) with $i = \sqrt{-1}$ and the complex relaxation function is $\widehat{G} = G' + iG''$. Repeating the convolution integration Equation (2.1) and neglecting the decaying part, gives the response as

$$\frac{\tau(t)}{\gamma_0} = [G' + iG''] e^{i\omega t} = [G' \cos \omega t - G'' \sin \omega t] + i [G' \sin \omega t + G'' \cos \omega t]. \tag{2.6}$$

The real part is the response to a cosine input, and the imaginary part is the response to a

[1]Complex-valued quantities are denoted with a hat, such as $\widehat{\gamma}$.

sine input. Moreover, the convolution integral Equation (2.1) can now be replaced by

$$\tau(t) = \widehat{G}(\omega)\,\gamma_0 e^{i\omega t} \tag{2.7}$$

in terms of complex variables, when one is only interested in the limit cycle response after transients have died out.

2.3.2 Hydrogel characterization

Rheometry measurements were performed on PVA-PEG-boronate hydrogels using a torsional dynamical mechanical analyzer with cone and plate platens (Figure 2.2A). In all cases the shear strain γ amplitude was 2 %, and frequency scans were performed between 0.1 and 100 rad/s. Hydrogels of 10 % PVA (89-98 kDa) for several different cross-linker (CL) concentrations $C = \{2.5, 5, 7.5, 10, 12.5, 15\}\%$ were examined. Each case was run on three or four samples at 25 °C.

As an example, the results of a 10 % CL hydrogel sample are shown in Figures 2.2B–2.2E. The angular frequency was converted to cyclic frequency (f in Hz) according to $\omega = 2\pi f$, and frequency results are shown on a logarithmic scale for clarity. In Figures 2.2B and 2.2C, the open symbols mark experimental data, and the solid lines are fits according to Equations (2.4b) and (2.4c). In this case, and all others, $G_\infty = 0$ was prescribed, since the G' was quite small at low frequencies (see the lefthand tail in Figure 2.2B). This means the hydrogel actually behaves more like a viscoelastic fluid than a viscoelastic solid.

The fits for G' and G'' are reasonably good. This was achieved by selecting time constants at equal increments along a logarithmic scale, $\tau_j = \{2^{-10}, 2^{-9}, \ldots, 2^2\}$, and then fitting the parameters ξ_j ($j = 1, 2, \ldots, 13$) and ΔG. For most of the hydrogel samples, an unconstrained fit resulted in a distribution of ξ versus $\log\tau$ (relaxation spectrum) that resembled a Gaussian distribution. Consequently, the relaxation spectra for all of the results herein were constrained to lie along a Gaussian distribution according to

$$\xi_j = \xi(\tau_j) = \xi_0 \exp\left[-\left(\frac{\log(\tau_j/\tau_0)}{\sigma_0}\right)^2\right], \tag{2.8}$$

where τ_0 is the mean time constant, σ_0 is the standard deviation (characteristic width) of the distribution, and ξ_0 is a normalizing constant to make $\sum_{j=1}^{N_\tau} \xi_j = 1$. The resulting spectrum is shown in Figure 2.2E. This reduced the number of fitting parameters down to only three $\{G_0, \tau_0, \sigma_0\}$ for each hydrogel sample. The only tradeoff is that $\tan\delta$ is somewhat over-predicted at very low frequencies (see Figure 2.2D).

A summary is provided in Figure 2.3, showing the trends of the three fitting parameters

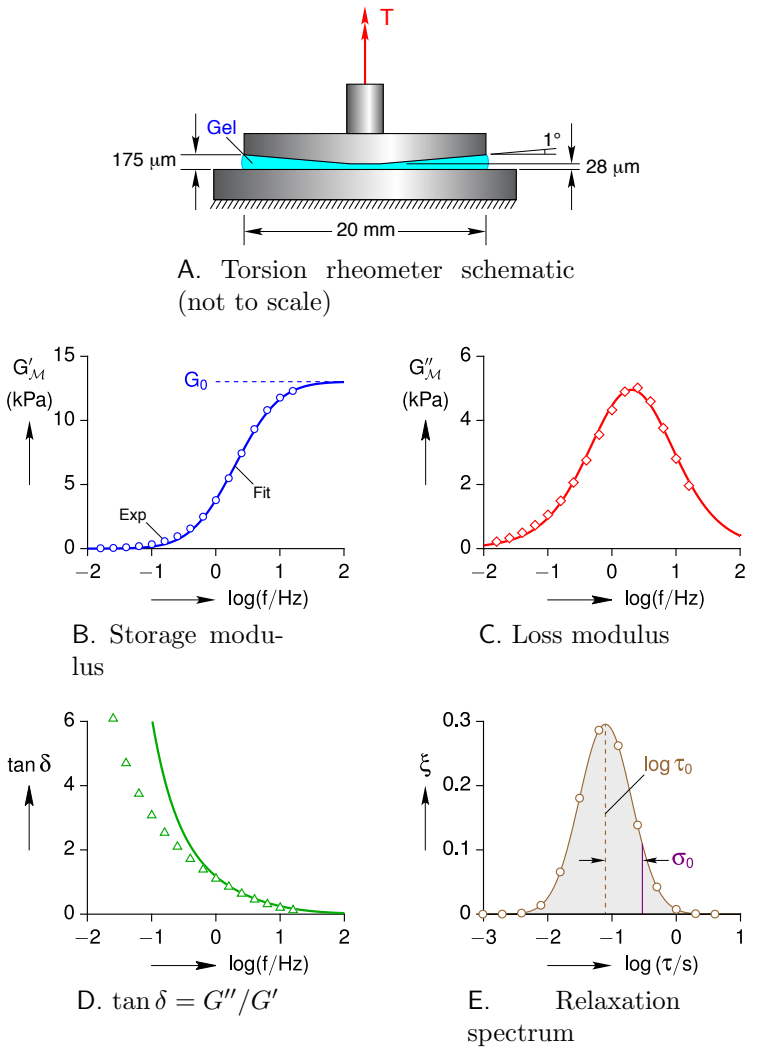

Figure 2.2: Example torsion rheology measurements on a $C = 10$ % cross-linked hydrogel. Solid lines are fits using a Gaussian relaxation spectrum.

across all CL cases. The data points shown were obtained by fitting each frequency scan, similar to Figure 2.2. The elastic shear modulus G_0 generally increases with CL concentration in a non-linear manner, although the scatter between samples becomes progressively larger. The mean time constant τ_0 also increases with CL concentration but trends almost linearly. The width of the relaxation spectrum σ_0 is nearly constant, except at the smallest CL concentration.

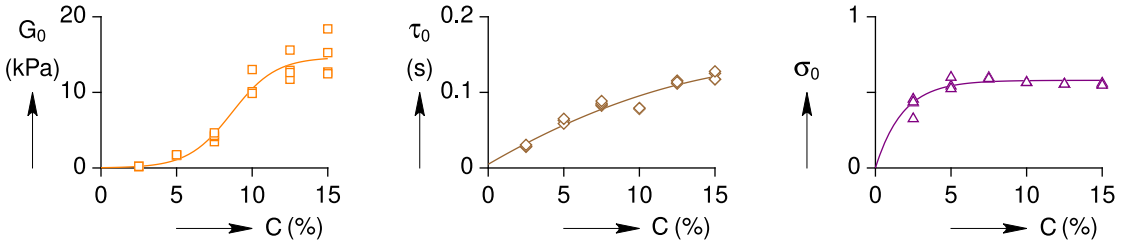

A. Elastic shear modulus

B. Mean time constant

C. Spectrum width

Figure 2.3: Summary of hydrogel viscoelastic parameters at different cross-link concentrations (C).

The lines in Figure 2.3 are CL-dependent fits of the fitting parameters according to

$$G_0(C) = \frac{g_0}{2}\left[1 + \tanh\left(g_1\left(C - g_2\right)\right)\right], \tag{2.9a}$$

$$\tau_0(C) = h_0 + h_1 C + h_2 C^2, \tag{2.9b}$$

$$\sigma_0(C) = s_0\left[1 - e^{-s_1 C}\right]. \tag{2.9c}$$

Values of the fitting constants are provided in Table 2.1. This resulted in master fit functions for the complex shear moduli as a function of frequency and CL concentration.

Table 2.1: Fitting parameters.

G_0	τ_0	σ_0
$g_0 = 14.7$ (kPa)	$h_0 = 0.00486$ (s)	$s_0 = 0.58$
$g_1 = 34.4$	$h_1 = 1.17$ (s)	$s_1 = 55$
$g_2 = 0.0866$	$h_2 = -2.62$ (s)	

2.3.3 Cardiomyocyte characterization

The elastic modulus of the cardiomyocyte was estimated using available data from the literature. [62] performed uniaxial force-stretch measurements on a single ventricular myocyte stimulated at 1.0 Hz frequency using coated micro-rods (Figure 2.4A). The cross-sectional area (A_0) of the gauge section of the myocyte between the rods was estimated from the micrograph assuming the out-of-plane depth was the same as the cell width, allowing the axial stress ($\sigma_{xx} = F_x/A_0$) to be calculated from the axial force (F_x). According to the extracted stress-strain response curve shown in Figure 2.4B, the cell had an approximate Young's modulus of $E^{\mathcal{I}} \approx 25$ kPa when electrically stimulated. Assuming the cell is an incompressible linear elastic solid, the effective shear modulus was $G^{\mathcal{I}} = E^{\mathcal{I}}/3 \approx 8.3$ kPa.

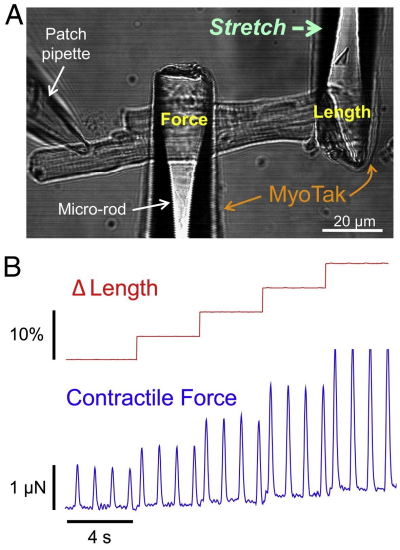

A. Figure from [62].

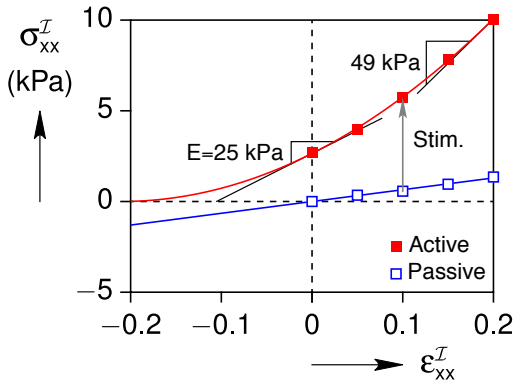

B. Estimated responses

Figure 2.4: Single cell uniaxial response.

To our knowledge, unfortunately, no viscoelastic data on a single cardiomyocyte currently exists in the literature.

2.4 Eshelby analysis

This section provides an analysis of the mechanical response of a live cardiomyocyte embedded in a viscoelastic hydrogel and paced to perform periodic beat-to-beat contraction. Our previous mechanical analysis of Cell-In-Gel experiments [58] was based on the Eshelby inclusion problem [56], where the cell was treated as an ellipsoidal inclusion that undergoes an eigenstrain (transformation strain) inside an infinite elastic matrix. The present work extends the Eshelby boundary value problem (BVP) to account for viscoelasticity of the constituents. Before the viscoelastic analysis is presented, however, a brief review is provided of the purely elastic Eshelby BVP.

2.4.1 Elastic Eshelby analysis

When the elastic properties in the inclusion and matrix are the same, the boundary value problem is called the *homogeneous* inclusion problem [56]. The inclusion occupies a subvolume $V^{\mathcal{I}}$, assumed here to have the shape of an ellipsoid, and is embedded and bonded to the matrix at its periphery (Figure 2.5). The matrix, occupying the complementary volume $V^{\mathcal{M}}$, is assumed to be of infinite extent, so the remote boundaries are traction and

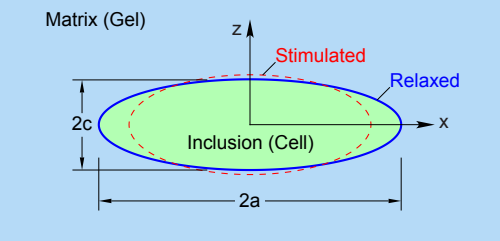

A. 2-D schematic

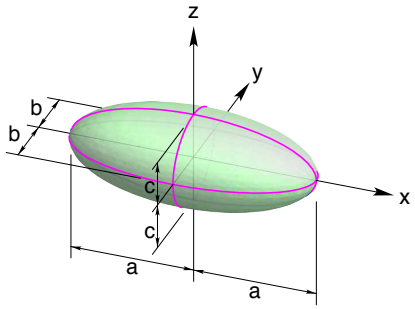

B. 3-D ellipsoidal inclusion

Figure 2.5: The Cell-in-Gel boundary value problem.

displacement free. The inclusion (here, the cell) is assumed to undergo an inelastic strain $\boldsymbol{\beta}$, called the eigenstrain. This simulates the strain of the cell when it contracts load-free (unconstrained by any matrix). The mechanical resistance of the matrix (here, the gel), however, causes the magnitude of the inclusion strain $\boldsymbol{\varepsilon}$ to be somewhat less. This tug-of-war causes self-equilibrated residual stress fields in the inclusion and the matrix.

With respect to the Cartesian coordinate system[2] shown in Figure 2.5b, the displacements u_i, strains ε_{ij}, and stresses σ_{ij} for the elasto-static problem are

$$u_i(\boldsymbol{x}) = B_{ijk}(\boldsymbol{x})\beta_{jk}, \tag{2.10a}$$

$$\varepsilon_{ij}(\boldsymbol{x}) = D_{ijkl}(\boldsymbol{x})\beta_{kl}, \tag{2.10b}$$

$$\sigma_{ij}(\boldsymbol{x}) = C_{ijkl}\left[\varepsilon_{kl}(\boldsymbol{x}) - \Gamma(\boldsymbol{x})\beta_{kl}\right], \tag{2.10c}$$

$$\text{with } \Gamma(\boldsymbol{x}) \equiv \begin{cases} 1, & \boldsymbol{x} \in V^{\mathcal{I}}, \\ 0, & \boldsymbol{x} \in V^{\mathcal{M}}, \end{cases} \tag{2.10d}$$

where $\boldsymbol{x} = x_i\boldsymbol{e}_i$ is the position vector with Cartesian components $\{x_i\} = \{x, y, z\}$ and orthonormal base vectors $\boldsymbol{e}_i$ $(i = 1, 2, 3)$. C_{ijkl} are the constant components of the 4th-

[2]Scalar quantities are denoted in normal type, while bold-face symbols denote vector or higher-order tensor quantities. The Einstein summation convention is used for repeated lower case latin subscripts within a term, as in $x_i\boldsymbol{e}_i = x_1\boldsymbol{e}_1 + x_2\boldsymbol{e}_2 + x_3\boldsymbol{e}_3$.

order elastic stiffness tensor $\boldsymbol{C}$. The quantities $B_{ijk}(\boldsymbol{x})$ and $D_{ijkl}(\boldsymbol{x})$ are position-dependent components of 3rd-order and 4th-order tensors, respectively, originally defined in [56, 57]. Within an ellipsoidal inclusion, the solution is

$$\varepsilon_{ij} = S^0_{ijkl}\beta_{kl}, \tag{2.11}$$

where $S^0_{ijkl} = D_{ijkl}(\mathbf{0})$ are the components of the classical Eshelby tensor $\boldsymbol{S}$. S^0_{ijkl} are constants, computed from elliptic integrals, which for isotropic material depend only on Poisson's ratio ν and the dimensions of the ellipsoid $\{a, b, c\}$. Thus, although strain and stress fields are quite non-uniform in the matrix, they are uniform within an ellipsoid inclusion (the only known shape for which this is true).

If the elastic properties of the inclusion $\boldsymbol{C}^{\mathcal{I}}$ and matrix $\boldsymbol{C}^{\mathcal{M}}$ are different, the BVP is called the *inhomogeneous* inclusion problem. It is solved by introducing an equivalent eigenstrain $\boldsymbol{\beta}^*$ that satisfies

$$\sigma^{\mathcal{I}}_{ij} = C^{\mathcal{I}}_{ijkl}\left[S^0_{klmn}\,\beta^*_{mn} - \beta_{kl}\right] = C^{\mathcal{M}}_{ijkl}\left[S^0_{klmn}\,\beta^*_{mn} - \beta^*_{kl}\right]. \tag{2.12}$$

The equivalent eigenstrain components β^*_{ij}, calculated from Equation (2.12), ensure the correct stresses are recovered after the inclusion elastic properties are replaced by those of the matrix $\boldsymbol{C}^{\mathcal{I}} \to \boldsymbol{C}^{\mathcal{M}}$. As shown in [56], this clever mathematical artifice converts any inhomogeneous inclusion problem to the homogeneous Eshelby problem (with its known analytical solution), and one just proceeds as before after replacing the actual eigenstrain by the equivalent eigenstrain ($\boldsymbol{\beta} \to \boldsymbol{\beta}^*$). Equation (2.10) then becomes

$$u_i(\boldsymbol{x}) = B_{ijk}(\boldsymbol{x})\beta^*_{jk}, \tag{2.13a}$$

$$\varepsilon_{ij}(\boldsymbol{x}) = D_{ijkl}(\boldsymbol{x})\beta^*_{kl}, \tag{2.13b}$$

$$\sigma_{ij}(\boldsymbol{x}) = C^{\mathcal{M}}_{ijkl}\left[\varepsilon_{kl}(\boldsymbol{x}) - \Gamma(\boldsymbol{x})\beta^*_{kl}\right]. \tag{2.13c}$$

For the Cell-in-Gel problem, the hydrogel (matrix) and cell (inclusion) are treated as isotropic and incompressible materials. The Young's modulus E and shear modulus G are related by $2G = E/(1+\nu)$, so in the limit $\nu \to 1/2$ the shear modulus is $G = E/3$. The dilatation in this case is zero ($\varepsilon_{kk} = 0$), and the deformation is isochoric (volume preserving). The eigenstrain components are taken as $\beta_{11} = \beta, \beta_{22} = \beta_{33} = -\beta/2$, and $\beta_{12} = \beta_{23} = \beta_{31} = 0$, where β is the eigenstrain along the cell's long axis. Explicit formulas for the computed equivalent eigenstrains can be found in [58]. The nonzero equivalent eigenstrains $\{\beta^*_{11}, \beta^*_{22}, \beta^*_{33}\}$ are proportional to β and depend nonlinearly on the ellipsoid dimensions and the shear modulus ratio $\eta \equiv G^{\mathcal{M}}/G^{\mathcal{I}}$. They are isochoric ($\beta^*_{kk} = 0$), and

$\beta^*_{12} = \beta^*_{23} = \beta^*_{31} = 0$. The stresses then become

$$\sigma_{ij}(\boldsymbol{x}) = 2G^{\mathcal{M}} \left[\varepsilon_{ij}(\boldsymbol{x}) - \Gamma(\boldsymbol{x})\, \beta^*_{ij}\right] + p(\boldsymbol{x})\, \delta_{ij}, \tag{2.14}$$

where the mean stresses in the inclusion and matrix are

$$p(\boldsymbol{x}) = \begin{cases} 3G^{\mathcal{M}} \beta^*_{11} \left[\dfrac{I_1(0)}{4\pi} - \dfrac{1}{3}\right], & \boldsymbol{x} \in V^{\mathcal{I}} \\ 3G^{\mathcal{M}} \beta^*_{11} \left[\dfrac{I_1(\lambda) - \Lambda(\lambda)\, x_1^2\, \alpha_1^2(\lambda)}{4\pi}\right], & \boldsymbol{x} \in V^{\mathcal{M}} \end{cases} \tag{2.15}$$

and expressions for $I_1(\lambda)$, $\Lambda(\lambda)$, $\alpha_1(\lambda)$, and $\lambda(\boldsymbol{x})$ are provided in [58].

The use of an ellipsoidal inclusion is reasonable, given that a typical cardiac cells is brick-like with jagged narrow ends in geometry. Using high-resolution finite element simulations, Kazemi-Lari *et al.* [42] recently showed that the strain and stress fields within a brick-shaped inclusion are no longer uniform (as expected), gently varying mostly along the inclusion's long axis. However, it was verified that the volume-averaged values of the stress components were reasonably similar between ellipsoidal and brick-shaped inclusion of the same aspect ratios.

2.4.2 Viscoelastic Eshelby analysis

Now we wish to account for the viscosity of the cell and gel in the framework of the Eshelby inclusion analysis. This causes all mechanical field quantities to become dependent on time t.

According to correspondence principle of linear viscoelasticity [61], if the linear elastic solution is known for a body that undergoes quasi-static motion, the solution to the corresponding problem in linear viscoelasticity can be constructed by substituting constitutive and load parameters with their time-dependent counterparts. The correspondence principle takes advantage of time-space separability by solving the time-dependent portion of the problem in the Laplace or Fourier domain. The principle however, is restricted to problems where the boundary location remains fixed in the reference configuration and boundary conditions do not change type over time. That is, while the surface tractions or displacements may be time-dependent, points on the surface must remain traction-specified, or displacement-prescribed, or displacement-traction coupled for all time. Ours is the last type.

The application of the correspondence principle has been used before to obtain the solution to the viscoelastic Eshelby inclusion problem in order to estimate the properties of composite materials. A recent paper [63] contains a summary of relevant papers. The ap-

plication of the viscoelastic Eshelby problem to cardiomyocytes in this paper is new.

Taking the Fourier transform of the field equations in Equation (2.13b), the pseudo-elastic solution is solved in the frequency domain by

$$\widehat{u}_i(\boldsymbol{x},\omega) = \widehat{B}_{ijk}(\boldsymbol{x})\widehat{\beta}^*_{jk}(\omega), \tag{2.16a}$$

$$\widehat{\varepsilon}_{ij}(\boldsymbol{x},\omega) = \widehat{D}_{ijkl}(\boldsymbol{x})\widehat{\beta}^*_{kl}(\omega), \tag{2.16b}$$

$$\widehat{\sigma}_{ij}(\boldsymbol{x},\omega) = 2\widehat{G}^{\mathcal{M}}(\omega)\left[\widehat{\varepsilon}_{ij}(\boldsymbol{x},\omega) - \Gamma(\boldsymbol{x})\,\widehat{\beta}^*_{ij}(\omega)\right] + \widehat{p}(\boldsymbol{x},\omega)\,\delta_{ij}. \tag{2.16c}$$

An arbitrary eigenstrain history can be expressed as the Complex Fourier Series

$$\beta(t) = \sum_{n=-\infty}^{\infty} \widehat{\beta}_n e^{i\,\omega_n t}, \tag{2.17}$$

where the coefficients are complex valued $\widehat{\beta}_n = \beta'_n + i\,\beta''_n$. Since $\beta(t)$ are real valued, the coefficients $\widehat{\beta}_n$ and $\widehat{\beta}_{-n}$ are complex conjugates.

The stress response to Equation (2.17) is just the superposition of responses at each individual frequency, since the viscoelastic constitutive relations and kinematics are linear. Thus, the generalization of Equation (2.16c) is the stress tensor (suppressing the spatial arguments)

$$\boldsymbol{\sigma}(t) = \sum_{n=-\infty}^{\infty} \widehat{\boldsymbol{\sigma}}_n e^{i\,\omega_n t}, \tag{2.18a}$$

$$\widehat{\boldsymbol{\sigma}}_n = \widehat{G}^{\mathcal{M}}_n\left[\widehat{\boldsymbol{\varepsilon}}_n - \Gamma\,\widehat{\boldsymbol{\beta}}^*_n\right] + \widehat{p}_n\,\boldsymbol{\delta}. \tag{2.18b}$$

where $\widehat{G}^{\mathcal{M}}_n = \widehat{G}^{\mathcal{M}}(\omega_n)$ is the complex relaxation moduli of the matrix at each frequency. This relation provides the steady state oscillatory response to a periodic eigenstrain input. The coefficient $\widehat{\beta}_n$ is found in the usual way by multiplying Equation (2.17) through by $e^{-i\,\omega_m t}$ with $\omega_m = 2\pi m/T$, integrating across the period of the interval $t \in [-T/2, T/2]$, and exploiting orthogonality of integrals involving $\exp(i2\pi(n-m)t/T)$, resulting in

$$\widehat{\beta}_n = \frac{1}{T}\int_{-T/2}^{T/2} \beta(t)\, e^{-i\,2\pi n t/T}\,\mathrm{d}t. \tag{2.19}$$

If the eigenstrain input is measured at N equal time increments ($\Delta t = T/N$) within the

period, the discrete sequence is

$$\beta_m = \beta(m\,\Delta t), \quad \text{for integers } m = -\frac{N}{2}, \ldots, \frac{N}{2} - 1. \tag{2.20}$$

which assumes N is even[3]. This leads to the Discrete Fourier Transform (DFT), where Equation (2.19) is approximated by

$$\widehat{\beta}_n \approx \frac{1}{N} \sum_{m=-N/2}^{N/2-1} \beta_m \, e^{-i\,2\pi nm/N}, \quad n = -\frac{N}{2}, \ldots, \frac{N}{2} - 1, \tag{2.21}$$

and the inverse DFT, replacing Equation (2.17), is

$$\beta_m = \sum_{n=-N/2}^{N/2-1} \widehat{\beta}_n \, e^{i\,2\pi nm/N}. \tag{2.22}$$

Finally, using Equation (2.18b) the stress response at discrete times becomes

$$\boldsymbol{\sigma}_m = \boldsymbol{\sigma}(m\,\Delta t) = \sum_{n=-N/2}^{N/2-1} \widehat{\boldsymbol{\sigma}}_n \, e^{i\,2\pi nm/N}. \tag{2.23}$$

Note that the ordering of frequencies needs to be done with care to ensure the complex modulus is summed over complex conjugate pairs. That is, we need $G'(\omega_n) = G'(-\omega_n)$ and $G''(\omega_n) = -G''(-\omega_n)$ when using Equation (2.4) with real frequency $\omega_n = 2\pi n/T$, which is why we prefer the quasi-symmetric summation about $n = 0$ (rather than the often used $n = 0, \ldots, N-1$).

Once the stress in the inclusion is known, the mechanical power output $P^{\mathcal{I}}$ of the cell (inclusion) can be calculated. This is related to the product of the instantaneous stress $\boldsymbol{\sigma}(t)$ and strain rate $\dot{\boldsymbol{\varepsilon}}(t)$in the cell, as

$$P^{\mathcal{I}}(t) = -\int_{V^{\mathcal{I}}} \sigma_{ij}(t)\dot{\varepsilon}_{ij}(t)\,\mathrm{d}V = -\sigma_{ij}(t)\dot{\varepsilon}_{ij}(t)V^{\mathcal{I}}, \tag{2.24a}$$

and the work done per cycle is

$$W^{\mathcal{I}} = \int_{t_0}^{t_0+T} P^{\mathcal{I}}(t)\,\mathrm{d}t. \tag{2.24b}$$

The volume of the ellipsoidal inclusion is $V^{\mathcal{I}} = (4/3)\pi abc$ (see Figure 2.5B), and t_0 is the

[3] If N is odd, $m = -\frac{N-1}{2}, \ldots, \frac{N-1}{2}$

start time of a cycle. One should recognize that $W^{\mathcal{I}}$ is the net mechanical work done by the cell on the gel, which is apart from other internal energy expenditures of the cell to maintain metabolic homeostasis, ionic homeostasis, and Ca^{2+} signaling.

The internal stress, strain, and strain rate provide volume-averaged values of relevant mechanical quantities that may be felt by interior mechano-sensors in the cell. Notably, the 3-D mechanical analysis also provides important clues to the locations of various mechano-sensors in the cell [52]. The mechanical loading sensed by surface mechano-sensors of the cell can be estimated by calculating the traction vector $\boldsymbol{t}^{\mathrm{e}}$ on the surface of the ellipsoid (interface of the cell and gel, $\partial V^{\mathcal{I}}$). The traction components are

$$t_i^{\mathrm{e}}(\boldsymbol{x}) = \sigma_{ij}^{\mathcal{I}}\, n_j(\boldsymbol{x}), \quad \boldsymbol{x} \in \partial V^{\mathcal{I}}, \tag{2.25}$$

where n_j are the components of the surface unit normal $\mathbf{n}$.

2.5 Simulation results

In this section, the results of our mechanical analysis are interpreted and compared to real biological data. The viscoelastic Eshelby model is used to calculate the multiaxial stress and strain states and the time-dependent mechanical responses of the cardiomyocyte contractions in the Cell-in-Gel experiments. First, simulation results are shown for a baseline case in the absence of MCT gain, which focuses on characterizing the mechanical field distributions inside and outside the cell. Next, a parameter study is performed to examine the influence of the hydrogel's viscoelastic properties, the cell's aspect ratio, and the cell's stiffness, on the cell's mechanical response. Finally, a feedback model is proposed and integrated into the mechanical analysis to incorporate the MCT gain and autoregulation of Ca^{2+} transients seen in the actual cardiomyocyte. This is shown to be an important ingredient to achieve good agreement between the simulations and the Cell-in-Gel measurements.

2.5.1 Baseline case

Consistent with the cardiomyocyte in the Cell-in-Gel experiment (Figure 2.1), the ellipsoidal inclusion has dimensions $2a = 131.2$ μm and $2b = 18.4$ μm, resulting in an aspect ratio of $a/b = 7.13$. From here on, in the absence of an out-of-plane measure, we assume $c = b$ for simplicity. This is a reasonable estimate for many myocytes, and our results are not greatly affected even if $c = 1.5b$ (as measured in certain myocytes.) The cell is treated as a contractile, elastic object with a shear modulus of $G_0^{\mathcal{I}} = 8.3$ kPa (consistent with Figure 2.4B) inside a viscoelastic hydrogel with $G_0^{\mathcal{M}} = 4.7$ kPa at a CL density of $C = 7.6$ %.

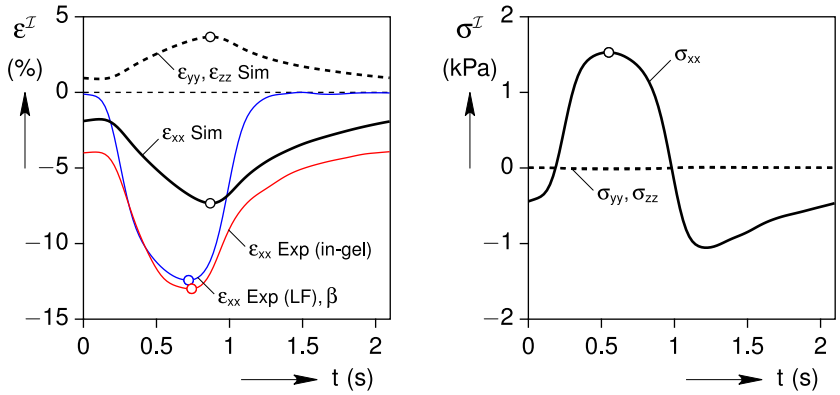

A. Strain histories B. Stress histories

Figure 2.6: Baseline case: cell strain and stress responses.

The Cell-in-Gel experiment recorded the axial strain history of a cardiomyocyte electrically stimulated at about 0.5 Hz after many cycles while embedded in the gel. A representative cycle, where $t = 0$ is the time of electrical stimulation, is shown in Figure 2.6A. The thin red line shows the in-gel strain history of the cell, with a maximum contraction near $\varepsilon^{\mathcal{I}}_{xx} = -13$ % strain. The gel was then dissolved away (leaving a nearly inviscid saline solution), and the strain history of the same myocyte was measured under nearly load-free conditions (thin blue line in Figure 2.6A). The maximum contraction in this case was slightly smaller, about -12.4 % strain. This load-free strain history is used as the eigenstrain input $\beta(t)$ in the viscoelastic Eshelby analysis of Section 4.3.

The predicted in-gel axial strain history (simulated ε_{xx}, shown by the bold black line in Figure 2.6A) has the right qualitative character, but the peak contraction (-7.3 % strain) is less than the experimental value (-13 %). As was shown in Figure 2.1C, the actual myocyte significantly upregulates its intracellular Ca^{2+} transient by the MCT mechanism to increase contractility in response to the mechanical load. This adaptive feature is not captured here in the Eshelby model which treats the cell as an MCT-free passive entity, but will be included in Section 2.5.3. Also, as expected for a contractile inclusion inside a viscoelastic gel, the times of peak eigenstrain, peak inclusion strain, and peak inclusion stress are somewhat different. The minimum eigenstrain β occurs at $t = 0.72$ s, while the maximum axial stress $\sigma^{\mathcal{I}}_{xx} = 1.53$ kPa occurs about 0.17 s earlier and the minimum axial strain $\varepsilon^{\mathcal{I}}_{xx}$ occurs about 0.15 s later. The minimum strain measured in the myocyte reaches its minimum value at $t = 0.74$ s which happens 0.13 s earlier than the simulated minimum axial strain $\varepsilon^{\mathcal{I}}_{xx}$. The stress state in the inclusion is multi-axial, but the peak lateral stresses are quite small (minimum $\sigma^{\mathcal{I}}_{zz} = -0.015$ kPa) due to the slenderness of the ellipsoid.

Selected field quantities in the cell and gel, including the displacements, longitudinal

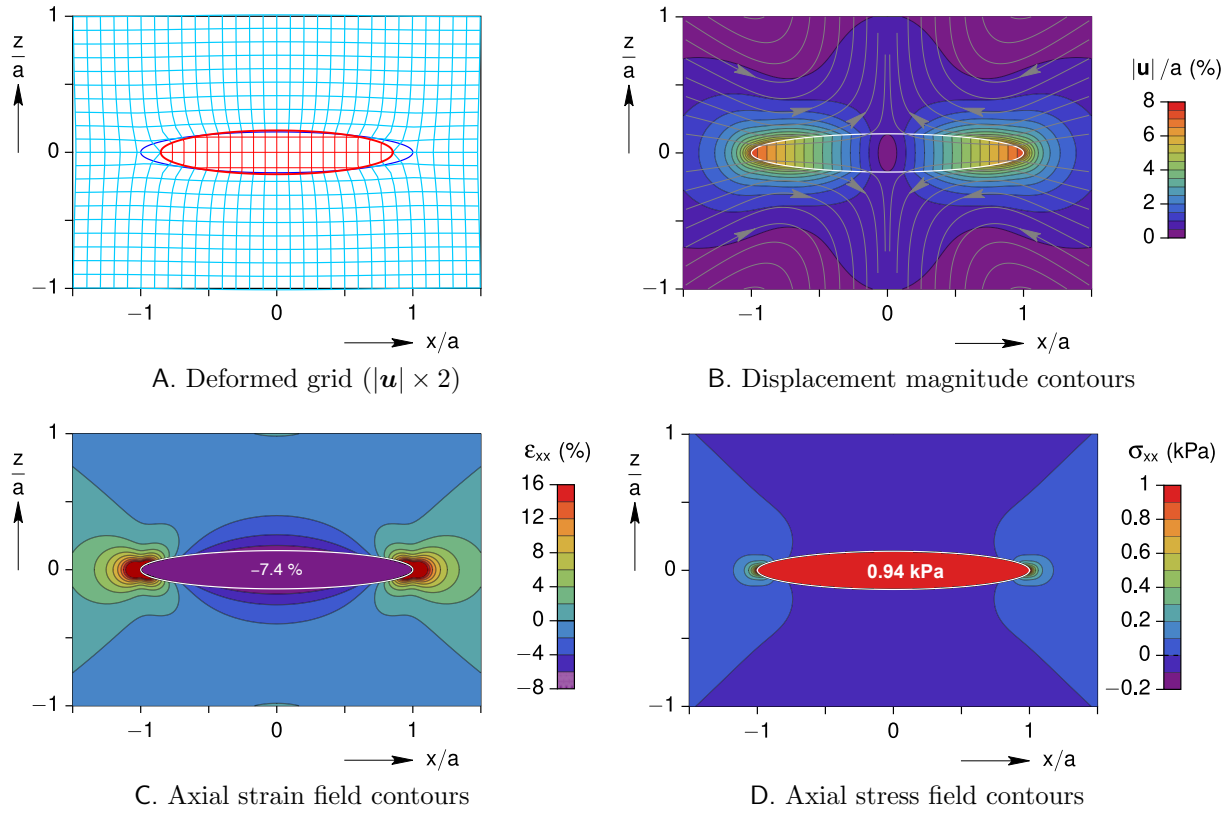

A. Deformed grid ($|\boldsymbol{u}| \times 2$)

B. Displacement magnitude contours

C. Axial strain field contours

D. Axial stress field contours

Figure 2.7: Baseline case: interior and exterior mechanical fields in the $y = 0$ plane at the time of minimum cell strain ($t = 1.1$ s).

strain, and longitudinal stress, are shown in Figure 2.7 at the time of maximum contraction within the symmetry plane $y = 0$. The problem is also symmetric with respect to the plane $x = 0$ (mid-span) and axisymmetric about the x-axis (since $b = c$). The stress and strain fields inside the cell (inclusion) are uniform at any given time instant. The fields in the gel (matrix), however, are non-uniform with a local strain and stress concentration just outside the cell's ends ($x = \pm a$), but these decay quickly to zero away from the cell.

Figure 2.7A shows a deformed grid, where the displacements have been magnified two-fold to clearly show the constrained cell which pulls on the surrounding hydrogel along the axial direction (x) yet pushes outward on the gel along the transverse direction (z). Figure 2.7B presents a contour plot of the magnitude of the displacement ($|\boldsymbol{u}|$) normalized by the cell's half-length (a). Streamlines are overlaid to show the directions of displacements during contraction, again showing how the gel is drawn inward toward the ends of the cell at $(x, y, z) = (\pm a, 0, 0)$, yet is pushed away from the cell at the mid-span $(0, 0, \pm c)$. The contour plot also shows that non-zero displacements in the gel are localized to the vicinity of the cell, and rapidly approach zero by $|\boldsymbol{x}| > 2a$, or so. Thus, the map provides useful information

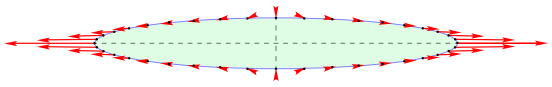

A. Cell tractions ($y = 0$ plane)

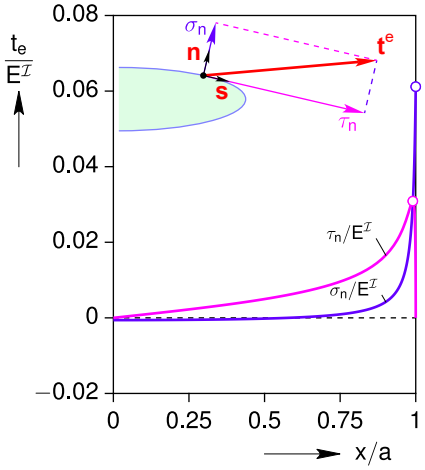

B. Normal & shear components

Figure 2.8: Baseline case: traction distribution along the cell boundary at the time of peak stress ($t = 0.55$ s).

about the expected displacements in the gel, which can be compared to the displacements of the micro-beads in the Cell-in-Gel experiments. Contour plots of the axial strain (ε_{xx}) and axial stress (σ_{xx}) are provided in Figures 2.7C and 2.7D, respectively, showing uniform strain and stress fields inside the cell. In the gel, both plots exhibit 'hot spots' near the cell ends and at the mid-span (although much less severe). The maximum stresses and strains in the gel are quite local, less than $a/4$ in extent near the cell ends.

To give a sense of the magnitude and direction of the traction along the boundary points, a scaled schematic of the traction vector distribution along the entire cell's boundary is provided in Figure 2.8A. A more quantitative view of the traction distribution is provided in Figure 2.8B, taken at the moment ($t = 0.55$ s) of peak cell stress ($\sigma^{\mathcal{I}}_{xx} = 1.53$ kPa). The traction vector $\boldsymbol{t}^{\mathrm{e}}$ on the surface of the ellipsoid is decomposed into normal σ_n and shear τ_n components relative to the surface (see inset schematic), and these are normalized by the Young's modulus of the cell $E^{\mathcal{I}}$. Because of the symmetry with respect to $x = 0$ and $z = 0$ planes, the traction components are only plotted in the positive quadrant of the $y = 0$ plane. The outward unit normal to the cell surface is $\boldsymbol{n}$, the tangential unit vector is $\boldsymbol{s}$, and they are orthogonal ($s_i n_i = 0$). Figure 2.8B shows that the normal component of the traction $\sigma_n = t^{\mathrm{e}}_i n_i$, acting perpendicular to the surface, changes from slight compression (over about 50 % of the length) to rapidly increasing tension, reaching a maximum value

of about $0.061E^{\mathcal{I}}$ at the cell end ($x = a$). The shear component of the traction $\tau_n = t_i^{\mathrm{e}} s_i$, acting tangent to the cell's surface, starts zero at the mid-span ($x = 0$) and rises across the length until it reaches a maximum of about 0.031 $E^{\mathcal{I}}$, before dropping sharply to zero at the cell end. Since the ellipsoid here is axisymmetric ($c/b = 1$), the same results would have been obtained if the tractions were plotted in the positive quadrant of any other plane that includes the x-axis.

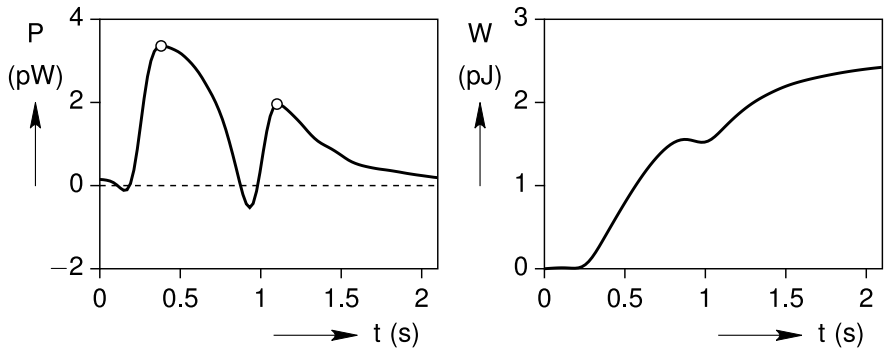

A. Mechanical power B. Mechanical work

Figure 2.9: Baseline case: cell output power and work histories.

Using Equation (2.24), the output power and work of the cell during one contraction cycle are quantified in Figure 2.9. Interestingly, the power history in Figure 2.9A exhibits two local maxima near $t = 0.38$ s at 3.36 pW (picowatts) and $t = 1.10$ s at 1.96 pW, due to the out-of-phase stress and strain histories. Integrated from the power, the corresponding mechanical work history is provided in Figure 2.9B. After a latency of about 0.2 s, the cell does positive work on the gel during systole, the gel momentarily does work against the cell as it decelerates, and then the cell again does work on the gel as the cell elastically lengthens during diastole. Overall, the (MCT-free) cardiomyocyte outputs a total work of $W = 2.42$ pJ/cycle during beat-to-beat contraction inside the viscoelastic hydrogel.

2.5.2 Parametric study

Numerous simulations were performed to understand the parametric sensitivities of the Cell-in-Gel system with respect to the gel crosslink (CL) concentration, the cell aspect ratio, and the cell stiffness. Each parameter is varied one at a time, while holding the other parameters fixed at their base case values. The viscosity of the cell itself was also investigated, but it had a relatively minor influence on the response so it is not shown. All cases calculated below use the same load-free eigenstrain history $\beta(t)$ as before.

As demonstrated in Figure 2.10A, the hydrogel's CL concentration (C) has a strong effect on the cell contraction. As C is increased, the predicted magnitude of cell's axial

strain is significantly reduced and the phase difference between the stimulus signal and the contraction response is increased. In addition, Figure 2.10B shows how the magnitude of the axial stress increases and the stress recovery becomes delayed with increasing C. Cross-plots of the corresponding stress-strain responses are provided in Figure 2.10C. Each response is a hysteretic loop, where the enclosed area is related to the (output) mechanical work done by the cell on the gel. The hysteresis is small at low CL concentration ($C = 2$ %), large at intermediate concentrations (6 %), and small again at large concentrations (10 %). The calculated output work per cycle is plotted in Figure 2.10D after normalizing by the cell volume to give a work density ($\widehat{W} = W/V^{\mathcal{I}}$). This shows that the work density starts at zero for $C = 0$, grows to a maximum value near 132 J/m^3 at $C = 6$ %, and then decreases for larger C. This non-monotonic trend is to be expected, since $W = 0$ at the two extremes, $C = 0$ (no gel, zero cell stress) and $C \to 1$ (nearly rigid gel, zero cell strain).

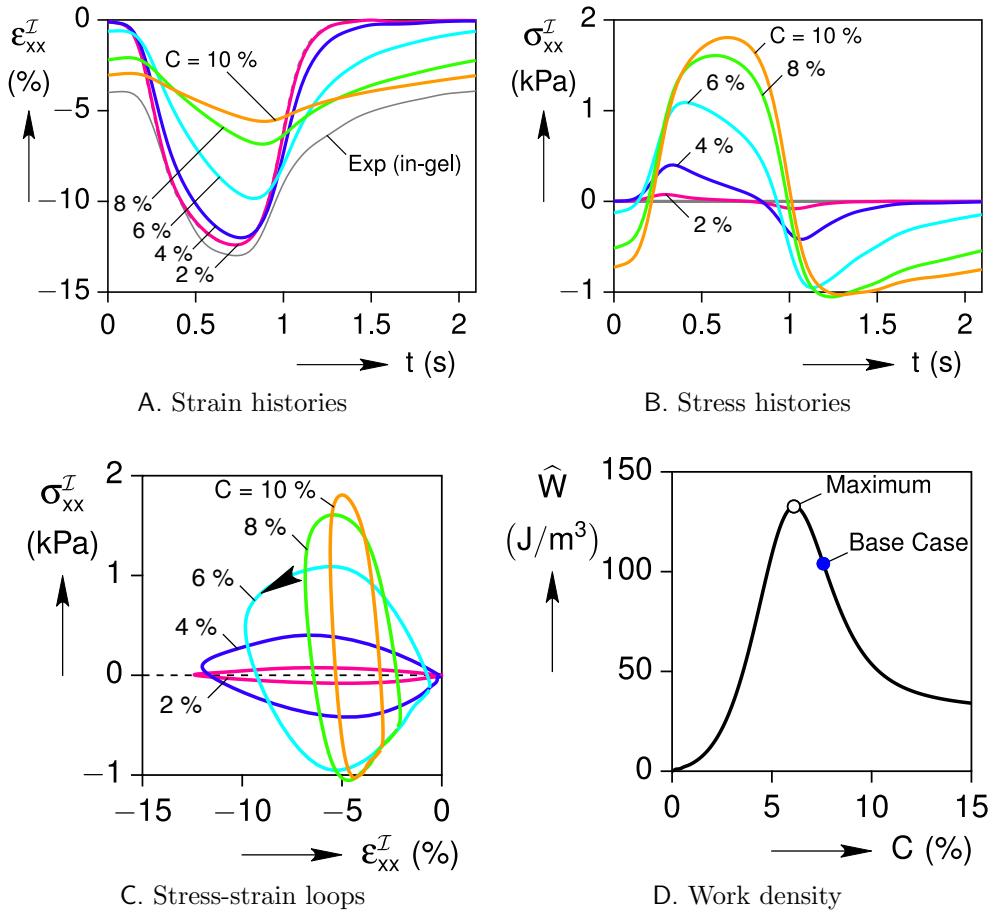

A. Strain histories B. Stress histories

C. Stress-strain loops D. Work density

Figure 2.10: Effect of gel's cross-link concentration C on the cell response ($a/b = 7.13$, $G^{\mathcal{I}} = 8.3$ kPa).

The effect of cell's aspect ratio has a similar non-monotonic effect on the cell response as

shown in Figure 2.11. As the cell becomes more slender (larger a/b), reduced contractions and larger stresses are predicted (Figures 2.11A and 2.11B). This trend can also be understood by examining the extreme cases. A spherical inclusion ($a/b = 1$) is the most able to contract, but its short length generates only a small displacement (for a fixed eigenstrain). A thin needle ($a/b \to \infty$) would not be able to contract at all, since its axial cross-sectional area tends to zero. Likewise, the axial force would become very small, and the cell's attempted contraction would be supressed by the resisting gel. As seen in Figures 2.11C and 2.11D, increasing the cell's aspect ratio from a small value ($a/b \approx 1$) initially causes the stress-strain hysteresis and work density to increase. The work density reaches a peak at about 125 J/m^3 at $a/b = 4$, and then decreases thereafter.

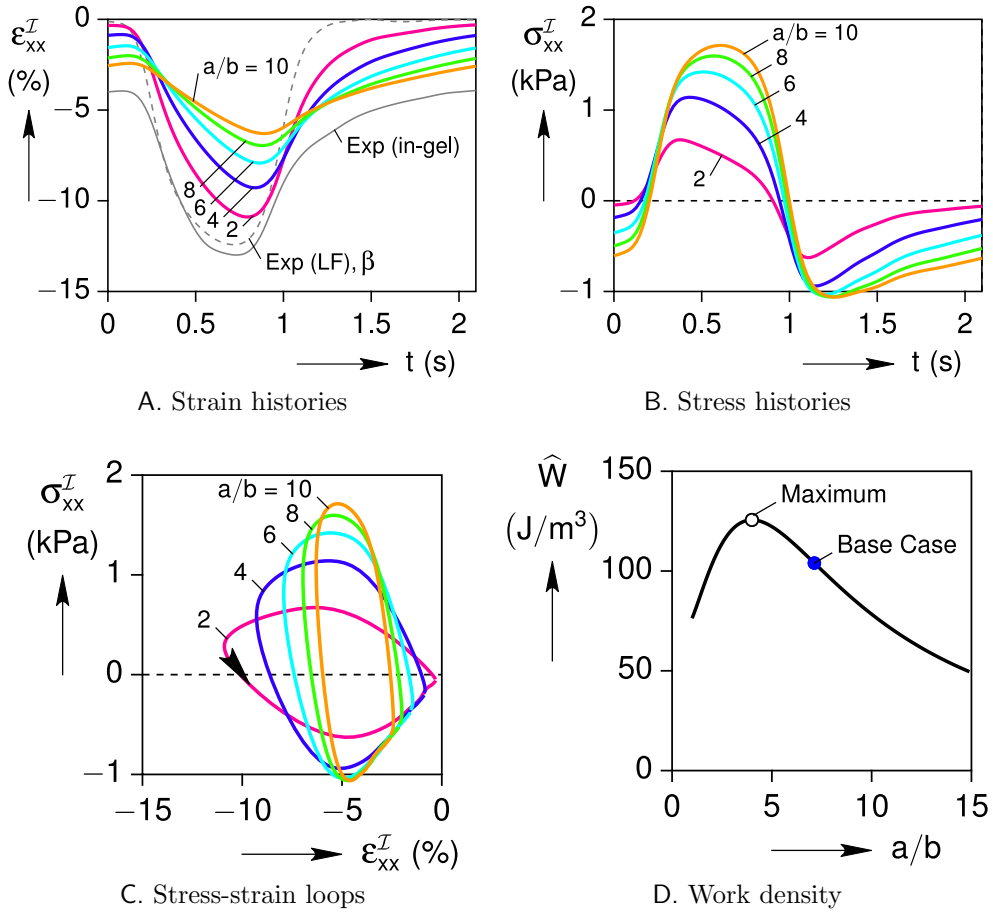

Figure 2.11: Effect of cell aspect ratio a/b on the cell response ($C = 7.6$ %, $G^{\mathcal{I}} = 8.3$ kPa).

The cell's shear modulus ($G^{\mathcal{I}}$), by contrast, has a monotonic influence as shown in Figure 2.12. A stiffer cell is able to contract more (Figure 2.12A), and this generates larger stresses (Figure 2.12B). The stress-strain loops (Figure 2.12C) and the work density (Fig-

ure 2.12D) become larger. This makes sense, as a relatively compliant cell ($G^{\mathcal{I}} \ll G_0^{\mathcal{M}}$) could not contract much against the gel, while a nearly rigid cell's contraction would approach the eigenstrain history, $\varepsilon_{xx}^{\mathcal{I}}(t) \to \beta(t)$.

Despite the wide range of parameters examined, none of the responses appear to approach the measured in-gel strain history of the actual cell. Admittedly, each parameter C, a/b, and $G^{\mathcal{I}}$ has an uncertainty. The crosslink concentration was measured carefully, but the viscoelastic properties do have some scatter (see again Figure 2.3). We also note that in the Cell-in-Gel experiment, the crosslinker had to be mixed in gently to avoid killing the myocytes, so it is possible that some spatial nonuniformity in CL concentration could have existed in the chamber. That, if anything, would have likely decreased the effective CL concentration, not increased it. The aspect ratio of the cell was measured optically, so we expect the in-plane aspect ratio is known reasonably accurately, although we could not measure the out-of-plane dimension. Based on the dimensions of many myocytes measured, one would not expect c to be much different than b, and even if it was 50 % different calculations show that it would not matter much. The elastic modulus of the cell is perhaps the parameter with the largest uncertainty, since we did not actually measure it (estimated from literature data [62] for a rodent ventricular myocyte) and is subject to unknown variability between myocyte isolations and animal species. Nevertheless, the range of $G^{\mathcal{I}}$ we considered appears to be extreme, and even in the case $G^{\mathcal{I}} \to \infty$ the calculation still did not trend to the experimental result.

The missing feature in our (MCT-free) simulations so far is that the actual myocyte clearly has an autoregulation in response to afterload (as observed in the intact heart). We can envision two possible mechanical manifestations, either the cell increases its elastic stiffness and/or the cell adapts its eigenstrain. Based on our results above, the discrepancy between our predictions and the actual myocyte's in-gel response cannot be explained by changes in the cell stiffness alone. The cell stiffness cannot change the delay in the peak contraction compared to the experimental in-gel strain history, and the calculation does not match the prolonged contraction decay in the actual strain history. It appears, therefore, that the autoregulation in response to afterload at the single cell level is primarily associated with an altered eigenstrain history.

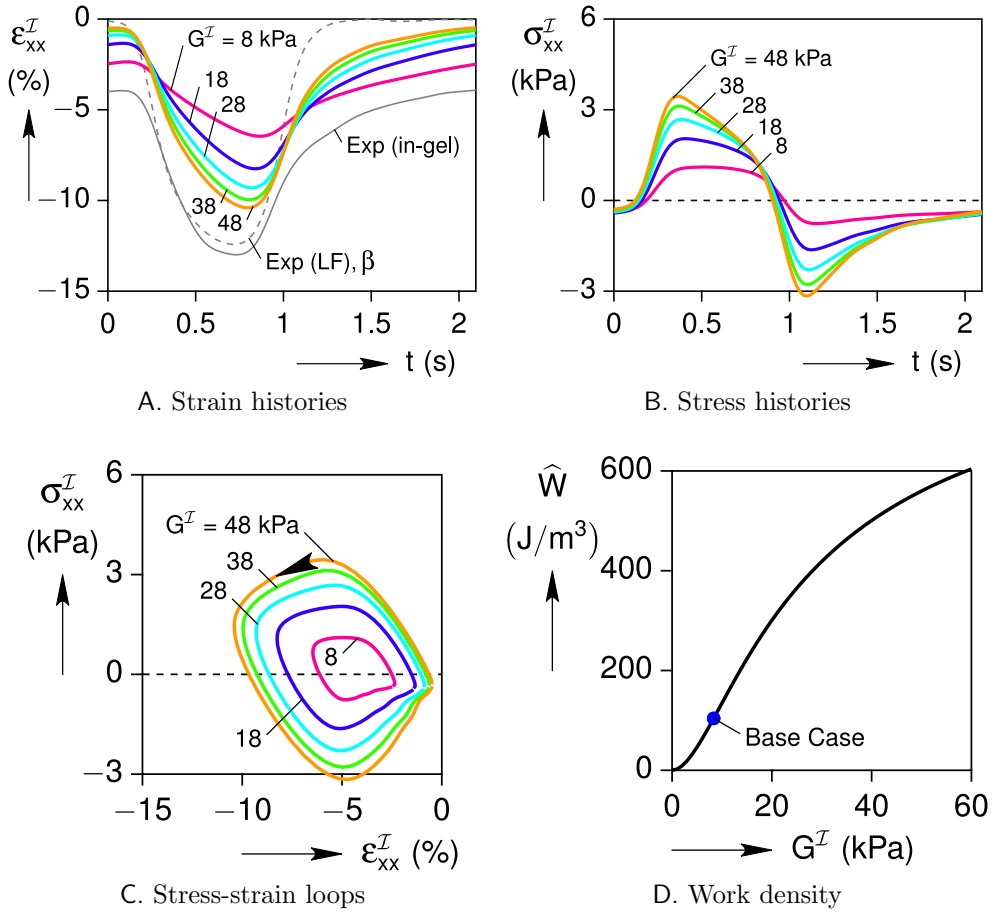

Figure 2.12: Effect of cell stiffness $G^{\mathcal{I}}$ on the cell response ($a/b = 7.13$, $C = 7.6$ %).

2.5.3 Autoregulation model

We hypothesize that the MCT mechanism effectively alters the eigenstrain history in response to the mechanical load on the cell. That is, the real cell can sense the increased load and increases the Ca^{2+} transient to enhance contractility. The MCT-Ca^{2+} gain is clearly observed in our experiments, but the exact MCT mechanism is incompletely understood. A well-calibrated mechanical analysis should provide clues that will inform the ongoing investigation of MCT mechanisms and functional consequences in cardiomyocytes.

Our approach to mathematically capture the cardiomyocyte's autoregulatory response is depicted in the block diagram of Figure 2.13. The complete feedback loop requires two additional mathematical "links" (shown in the bold green boxes) to the VE Eshelby analysis. The first link is the known enhancement of contractility due to the amplified Ca^{2+} transient (Ca^{2+}Contractility Coupling), and the second is the Ca^{2+} gain due to the self-sensed afterload (Stress-Ca^{2+} MCT). Each is described below.

Ca^{2+}-Contractility Coupling: This first link is described by the following first-order ki-

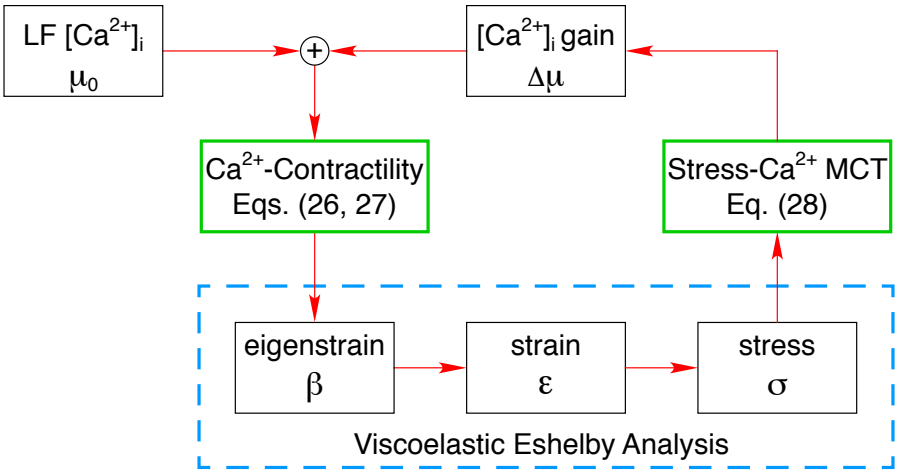

Figure 2.13: Control loop diagram for autoregulation of cardiomyocyte contraction to afterload.

netic model that connects the cytosolic Ca^{2+} concentration $\mu = \left[Ca^{2+}\right]_i$ to the eigenstrain β (contractility),

$$\beta(t) + a_1\dot{\beta}(t) = f[\mu(t)], \quad 0 \leq t < T, \tag{2.26}$$

where a_1 is a time constant, $f[\mu(t)]$ is a functional of the Ca^{2+} transient $\mu(t)$, and the initial condition is $\beta(0) = 0$ at the start of the cycle. The right-hand side of Equation (2.26) is a "forcing function" (f), chosen to capture the system dynamics. Figures 2.14A and 2.14B show measured time histories of the strain and Ca^{2+} respectively, comparing load-free and in-gel responses. Recall that the experiment in Figure 2.1 began with the cell contracting in the cross-linked gel and then the crosslinker was dissolved, allowing the cell to contract in Tyrode's solution (essentially load-free). It should be emphasized that the figure shows representative cycles for each case (in-gel and load-free) measured on the same cell, and this provides a direct comparison that avoids complications from cell-to-cell variability. As noted earlier, Figure 2.14A shows that the cell achieves an even slightly larger contraction in-gel than when load-free. Due to the presence of the gel, however, the cell is unable to fully recover its deformation and a residual strain of almost -4 % remains at the end of each cycle. The in-gel Ca^{2+} oscillations exhibit an MCT gain ($\Delta\mu \approx 1$) compared to the load-free case in Figure 2.14B, indicating a significant upregulation of the intracellular Ca^{2+} transient, as measured by the standard Fura-2 fluorescence ratiometric method [55]. Cross-plots of strain versus Ca^{2+} for the LF and in-gel cases are provided in Figure 2.14C, showing a much larger hysteresis for the in-gel case.

From the observed behaviors in Figure 2.14, the following nonlinear function is proposed

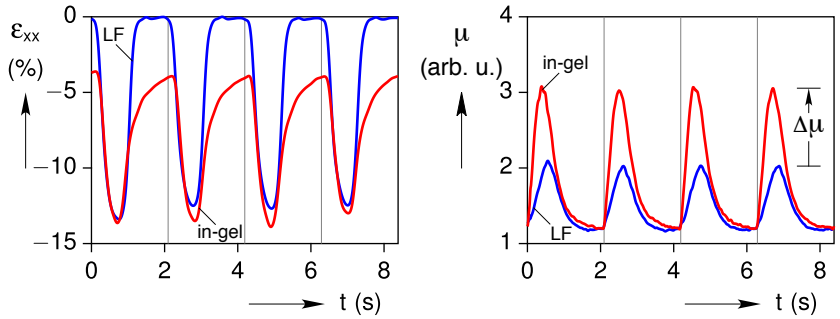

A. Measured strain histories

B. Measured Ca^{2+} histories

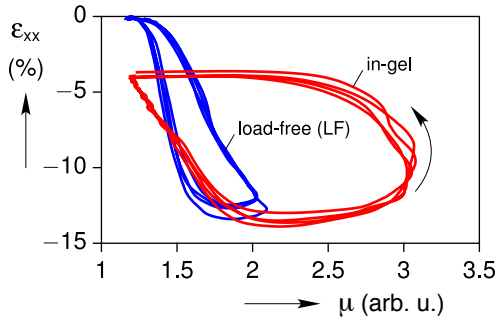

C. Strain-Ca^{2+} loops

Figure 2.14: Comparison of load-free (LF) and in-gel responses from the gel-dissolve experiment of Figure 2.1.

for f,

$$f[\mu(t)] = \frac{-b_0\,\bar{\mu}}{1 + b_1\,e^{-b_2[\mu(t)-\bar{\mu}]}}\mu(t), \tag{2.27a}$$

$$\bar{\mu} = \frac{1}{T}\int_0^T \mu(t)\mathrm{d}t, \tag{2.27b}$$

where $\bar{\mu}$ is the average of the Ca^{2+} transient during one actuation cycle and $\{b_0, b_1, b_2\}$ are positive constants. The magnitude of f in Equation (2.27a) is essentially proportional to $\mu(t)$ when $\mu(t) > \bar{\mu}$, yet $f \approx 0$ when $\mu(t) < \bar{\mu}$ due to the exponential in the denominator getting large. The resulting response is very nearly periodic, $\beta(0) = \beta(T)$, since we choose a small value for a_1 ($a_1 \ll T$) and $f \approx 0$ during the last half of the time interval.

Overall, the coupled eigenstrain-Ca^{2+} model in Equations (2.26) and (2.27) has four parameters $\{a_1, b_0, b_1, b_2\}$. Identification of these parameters was done recursively using a numerical nonlinear least-squares minimization algorithm in Mathematica [64]. The model parameters were first calibrated to the measured load-free axial strain and Ca^{2+} histories, giving the values in Table 2.2. The resulting model was then tested using the measured

in-gel Ca^{2+} history to predict the upregulated eigenstrain.

Table 2.2: Eigenstrain-Ca^{2+} parameter values.

a_1 (s)	b_0	b_1	b_2
0.100	0.046	6.507	20.986

Figure 2.15 demonstrates an excellent fit of the model's load-free eigenstrain, β_{LF} (dashed blue line), against the experimentally measured load-free axial strain, Exp $\varepsilon_{\mathrm{LF}}$ (solid blue line). The load-free eigenstrain is the calculated response of the model, Equations (2.26) and (2.27), to the load-free Ca^{2+} transient in Figure 2.14B. The upregulated eigenstrain of the model, β_{MCT}, in Figure 2.15 is the calculated response of the model to the in-gel Ca^{2+} transient of Figure 2.14B. This accounts for mechano-chemo-transduction, which produces a peak MCT eigenstrain of -24 % compared to the peak load-free (MCT-free) eigenstrain of -13 %. It also produces a faster transient, with the peak β_{MCT} occurring about 0.2 s sooner. Thus, the contractility of the cell is enhanced in both its amplitude and rate.

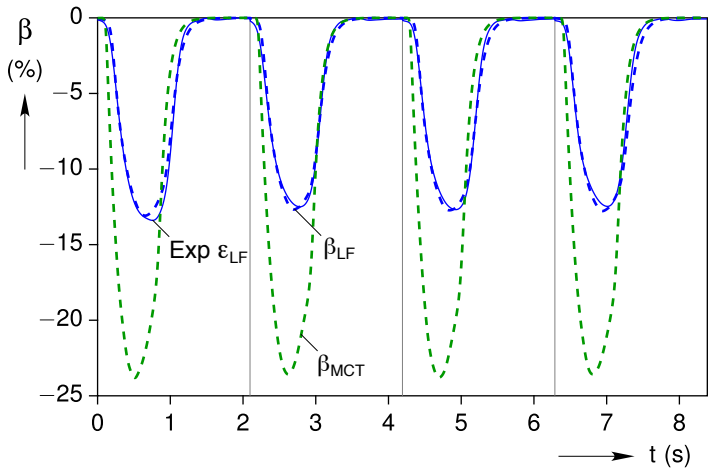

Figure 2.15: Simulated histories (dashed lines) of the load-free and MCT eigenstrains (β) calculated from Equations (2.26) and (2.27).

Using the predicted MCT eigenstrain (β_{MCT}), the baseline study simulation is repeated to capture the influence of Ca^{2+} upregulation on the cell deformation and stress. Figure 2.16 shows the simulated upregulated ($\varepsilon_{\mathrm{MCT}}$) axial strain and stress histories during a periodic cycle. Peak strains and stresses are identified with unfilled circles. The previous MCT-free simulated results (gray lines) are shown for reference. The agreement is now much better between the measured and simulated strain histories in Figure 2.16A. The magnitude of the simulated peak contraction is much closer and the time lag discrepancy is only 0.04 s.

Importantly, the maximum predicted axial stress resulting from the MCT eigenstrain is almost twice the MCT-free case in Figure 2.16B.

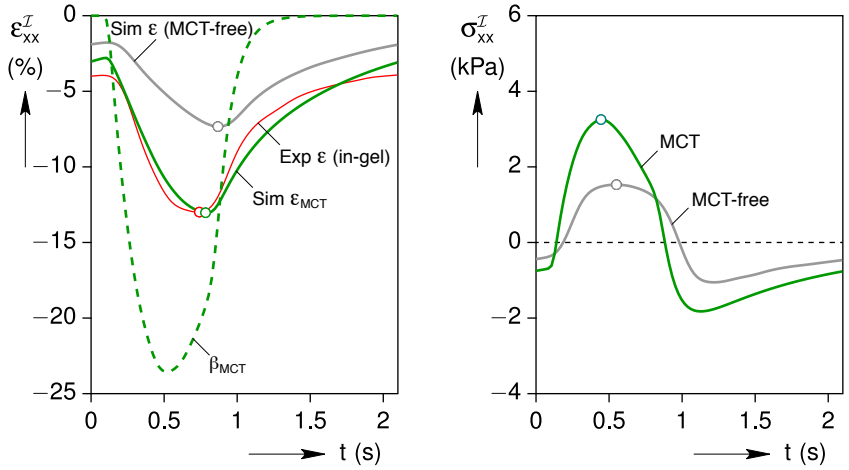

A. Axial strain histories

B. Axial stress histories

Figure 2.16: In-gel simulated cell strain and stress responses with (MCT) and without (MCT-free) Ca^{2+} upregulation.

With regard to the mechanical energy, the effect of MCT upregulation is even more significant. A comparison of the mechanical power and work histories between the MCT and MCT-free simulations are plotted in Figure 2.17. The increases in mechanical power and work are quite large, since the strain magnitude, strain rate, and stress magnitudes are all enhanced in the MCT model. The calculated mechanical work delivered by the upregulated cell at the end of a cycle is $W = 8.53$ pJ, which is about 3.5× larger than the MCT-free cell.

Stress-Ca^{2+} MCT: To complete the feedback loop, this second link relates the sensed afterload to the increase in Ca^{2+} transient. As mentioned earlier, we do not yet know the molecular identity or location of cell mechanosensors. For simplicity, our phenomenological model assumes that MCT-Ca^{2+} gain is a function of the cell's internal axial stress, since this is the dominant stress component and the stress is uniform throughout the ellipsoid. Accordingly, the input of the proposed model is the time-dependent MCT-upregulated axial stress, $\sigma^{\mathcal{I}}_{xx}$, and the output of the model is the increase in Ca^{2+} transient, according to,

$$\Delta\mu(t) + c_1\dot{\Delta\mu}(t) = \frac{d_0\,\left[\sigma^{\mathcal{I}}_{xx}(t) + d_1\right]}{1 + t^4\left[\sigma^{\mathcal{I}}_{xx}(t) + d_1\right]/d_2}, \tag{2.28}$$

where $\Delta\mu = \mu_{\mathrm{MCT}} - \mu_{\mathrm{LF}}$ is the difference (MCT gain) between the in-gel and load-free cytosolic Ca^{2+} in Figure 2.14B at every moment and $\{c_1, d_0, d_1, d_2\}$ are four constant parameters. The calibrated parameters of the proposed model for the current cell, identified

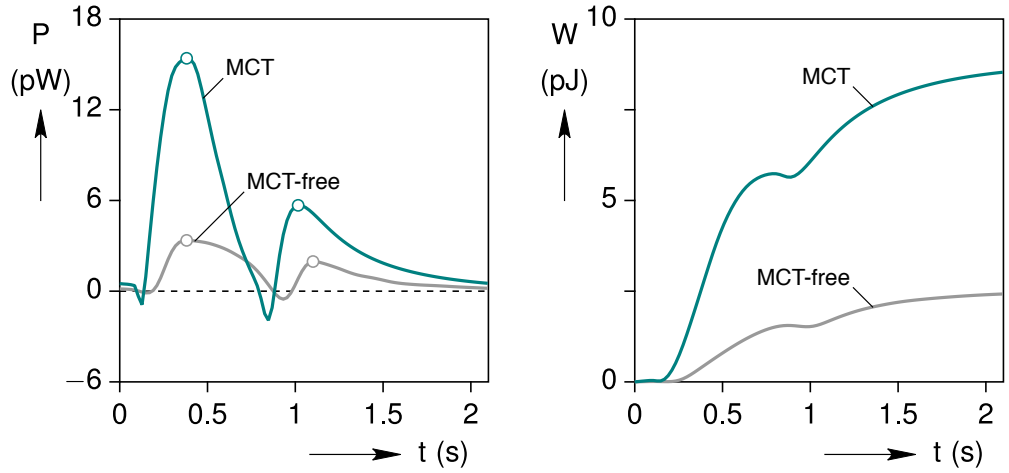

A. Power histories B. Work histories

Figure 2.17: Simulated mechanical power and work output of the cell with (MCT) and without (MCT-free) upregulation of Ca^{2+}.

recursively, are listed in Table 2.3. The quantity in brackets on the right-hand side is always positive due to the addition of d_1 to the cell stress. Note also the explicit time dependence (t^4) in the denominator on the right-hand side which grows large as time progresses and drives the right-hand forcing function to zero.

Table 2.3: Ca^{2+} gain-stress parameter values.

c_1 (s)	d_0	d_1 (kPa)	d_2 (kPa s^4)
0.18	0.37	3.37	0.10

Figure 2.18 compares the Ca^{2+} gain of the model with experimentally measured data. The predicted time-dependent Ca^{2+} gain ($\Delta\mu$), by a numerical solution of Equation (2.28), matches well with the measured history (Figure 2.18A). It is also worth mentioning that the MCT-upregulated axial stress inside the cell (Figure 2.16B) leads the Ca^{2+} gain time-response by about 0.06 s. The resulting Ca^{2+} gain versus the (simulated) cell axial stress in Figure 2.18B exhibits an oddly hysteretic response, but the important segment in the response appears to be the rising, nearly linear, portion (with the arrow).

With these two proposed links established, the MCT process forms a closed-loop wherein the mechanical force is sensed by the cell's mechanosensors and in response the cytosolic Ca^{2+} transient is increased by $\Delta Ca^{2+}(t)$. The upregulated Ca^{2+} transient in turn, magnifies the eigenstrain (β-MCT) and enhances the contractility of the cell.

Cell Viscoelasticity: Until now, the cell's passive mechanical properties have been modeled as purely elastic, but even better agreement with the experimental data can be achieved

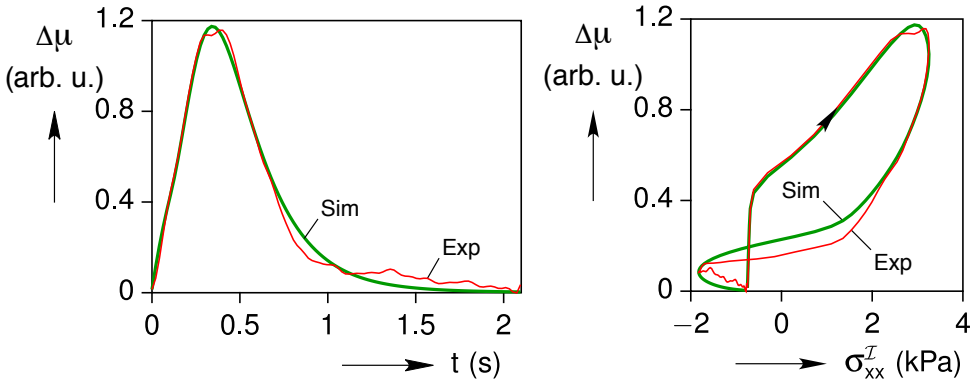

A. Ca^{2+} gain history

B. Ca^{2+} gain-stress loop

Figure 2.18: Comparison of the measured Ca^{2+} gain to the in-gel MCT simulation calculated from Equation (2.28).

by incorporating the viscosity of the cell itself (Figure 2.19). This final step is of secondary importance compared to the effect of upregulation, and it is somewhat speculative since we could not directly measure the viscosity of the cell. In the absence of better information, we chose the simplest possible viscoelastic constitutive model, a three-parameter viscoelastic solid (Equation (2.3) with $N_\tau = 1$) with $G_0^{\mathcal{I}} = 9.6$ kPa, $G_\infty^{\mathcal{I}} = 4.0$ kPa, and $\tau_1^{\mathcal{I}} = 0.6$ s. The same β_{MCT} from Figure 2.16A is used as the input to the simulation. As seen in Figure 2.19A, this produces a remarkably good match with the measured strain response of the cell (see $0.4 \text{ s} < t \leq 2.1$ s), such that the calculated peak strain of $\varepsilon_{xx}^{\mathcal{I}} = -12.9$ % is quite close to the measured value of -13.0 % and the time lag discrepancy is almost eliminated. The fact that the simplest possible viscoelastic model generates such good agreement provides us confidence that the assumed parameter values are reasonable and the important effects of the cell's viscosity are captured. Accordingly, Figure 2.19B provides our best estimate of the MCT cell's axial stress history during the in-gel portion of the Cell-in-Gel experiment. The peak stress of $\sigma_{xx}^{\mathcal{I}} = 3.27$ kPa occurs at $t = 0.40$ s, and the minimum stress (maximum compression) of $\sigma_{xx}^{\mathcal{I}} = -2.18$ kPa occurs at $t = 1.06$ s.

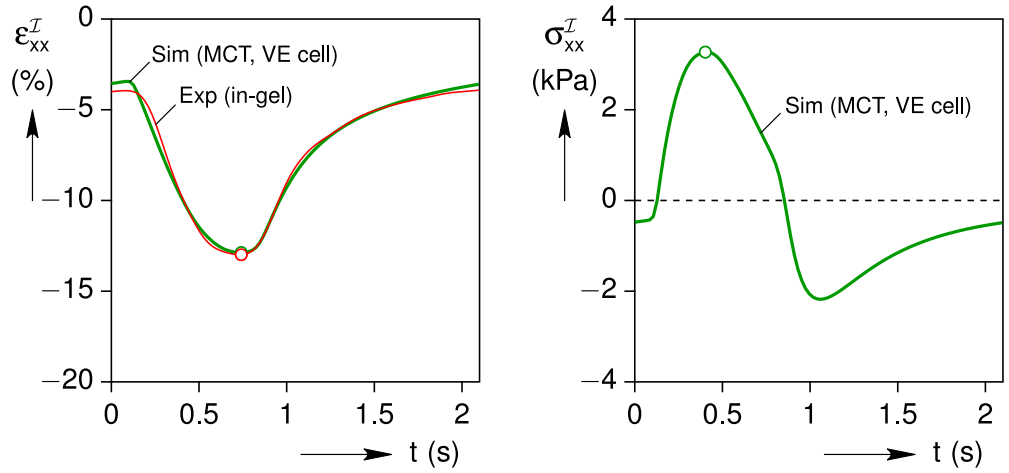

A. Axial strain histories

B. Axial stress history

Figure 2.19: Simulated MCT cell strain and stress responses (in-gel) including cell viscoelasticity, showing good agreement with the measured cell strain response.

2.6 Conclusions and perspectives

This study developed a computationally efficient mathematical model to analyze all mechanical fields associated with the contraction of a single cardiac muscle cell in an infinite viscoelastic medium. The mathematical model is based on the inhomogeneous Eshelby inclusion problem, a classical 3-D elasticity boundary value problem with a known exact analytical solution. By exploiting the Correspondence Principal of Viscoelasticity, the model is extended here, for the first time, to account for the viscoelastic properties of the cell and the surrounding hydrogel as used in ongoing Cell-in-Gel experiments. The model simulates the cardiomyocyte as a contractile ellipsoid embedded in an infinite 3-D viscoelastic medium and produces an exact solution of the time-dependent mechanical fields.

The existence of an analytical solution, along with a discrete Fourier transform of the periodic contractions, provides an efficient computational tool to quantify the periodic time histories of displacement, strain, and stress fields inside and outside of the cell. In particular, the stresses in the cell and gel, not directly measurable in the Cell-in-Gel experiments, must be inferred by analysis. The ability to accurately quantify the mechanical stress in the cell now makes it feasible to answer the important question "how much stress in a cardiomyocyte is a lot?" It also allows the mechanical energy and output power requirements of the myocyte under afterload to be quantified. The parametric study herein shows that the strain, stress, and mechanical work of the cell are significantly influenced by the viscoelastic properties of the gel and the aspect ratio of the cell (slenderness). While the internal strain and stress fields within an ellipsoidal cell are uniform (or nearly so in an actual myocyte) at any time

instant, the surface traction is strongly non-uniform with a distinct maximum near the ends (near intercalated discs).

The viscoelastic inclusion model can provide quantitative predictions of the mechanical properties and behavior of live biological cells with an active autoregulation mechanism. For example, the geometry and stiffness of the cardiomyocytes are determined by the cell type and pathophysiological state. In particular, mammalian ventricular myocytes are stout; whereas, atrial myocytes tend to be slender [65, 66]. In addition, the cell's stiffness may change during development, aging, or with genetic mutations [67, 68, 69]. Moreover, the multiaxial strains and stresses inside the cell are expected to influence internal mechanosensors such as titin [70], while the surface traction and transverse compression are expected to influence surface mechanosensors such as dystroglycans and integrins [71]. Furthermore, genetic mutations of some mechanosensors such as dystroglycans are known to cause muscular dystrophy cardiomyopathy [72, 73]. The comprehensive mechanical analysis of the 3-D strains and stresses in cardiomyocytes provided by this model is therefore useful to understand how the cell might sense multiaxial stresses, activate various mechanosensors, and transduce the strains and stresses to biochemical signals to regulate the heart's function.

Cell-in-Gel experiments show that a healthy cardiomyocyte can adapt to increased afterload by upregulating the cytosolic Ca^{2+} transient to enhance contractility. The developed viscoelastic Eshelby model initially assumed the cell to be a contractile but otherwise passive (MCT-free) inclusion, and it analyzed the in-gel cell response based on the load-free cell strain history (eigenstrain). Discrepancies between the simulated and measured strain timing and amplitude in-gel, however, led us to introduce an enhanced MCT-eigenstrain. The eigenstrain history was made dependent on the measured cytosolic Ca^{2+} transients through a proposed first-order differential equation. The model's parameters were calibrated using the load-free strain and Ca^{2+} measurements, and then the model was used to predict the MCT-eigenstrain history based on in-gel Ca^{2+} measurements. Using this upregulated eigenstrain, the viscoelastic Eshelby model then accurately predicted the enhanced contractility of the cell in response to afterload. Moreover, in an effort to complete the autoregulation (feedback) loop, another first-order differential equation model was introduced to provide a link between the mechanical stresses and the increase in Ca^{2+} transient during each contraction. The model provides a computational tool to investigate the cardiomyocyte autoregulatory response to external mechanical loads.

To summarize, the important contributions of this work are two-fold. The first is the application of the viscoelastic Eshelby inclusion problem to the Cell-in-Gel system. The second contribution is the development of a new mathematical feedback framework to account for the MCT mechanism in cardiomyocytes in response to afterload. The viscoelastic inclusion

model developed here provides a rigorous 3-D mechanical analysis to inform biological studies of the cellular and molecular mechanisms that enable the heart to autoregulate contractility under physiological loads but fail under pathological conditions in heart diseases.

CHAPTER 3

Inflation of Circular Rubber Membranes With Nonuniform Thickness and Material Properties

3.1 Introduction

Inflatable structures have gained considerable attention recently due to the growing demand for lightweight and low-cost structures. These structures possess an exceptionally high mechanical packaging efficiency and very small stowage volume, which gives them a wide scope of applicability ranging from space deployable structures, such as scientific balloons [74], antenna reflectors [75, 76, 77, 78], solar arrays [79], inflatable rovers [80, 81], re-entry and descent technology [82], human habitats [80, 83], and other implementations in automotive and civil engineering industries [84, 85, 86].

Of particular interest, is to achieve a desired shape upon inflation in order to meet certain criteria or perform a specific task. Green and Adkins [87] were among the first to use the theory of nonlinear membranes to study the problem of inflating an initially flat circular membrane. Their formulation consisted of using eight ordinary differential equations to determine eight unknowns numerically using a trial-and-error approach to a two-point boundary value problem. Yang *et al.* [88] extended this study to investigate other simplified solution approaches for finding the axisymetric deformation of nonlinear membranes through only three first-order ordinary differential equations with explicit derivatives. They used the equilibrium equations in the meridian, tangential and normal directions and employed the Mooney-Rivlin constitutive model to simulate the response of three different axisymmetric membrane structures, inflation of flat membrane, longitudinal stretching of a tube, and flattening of a semispherical cap. Feng *et al.* [89], later extended their previous work to study the response of nonlinear axisymmetric membranes using the principle of minimum potential energy in the framework of the Ritz method. They also explored the non-axisymmetric inflation of rectangular membranes in the context of the principle of minimum potential

energy using a series of kinematically admissible functions to approximate the deformed configuration [90].

Although the above mentioned solution methodologies were successfully implemented, their application was limited to simple geometries. Oden [91] and coworkers were the first to use the finite-element method in the context of large deformation membrane problems. They used flat triangular elements to discretize the domain. Later, Leonard and Verma [92] extended the developed theory to curved membrane elements and obtained good results for axisymmetric membrane inflation problems. Free and constrained inflation of elastic membranes in relation to thermoforming processes was studied both experimentally and numerically by Charrier *et al.* [93, 94] for axisymmetric and non-axisymmetric problems. They experimentally investigated the large-deformation pressure inflation of heated polymeric membranes against relatively cold mold surfaces and presented a finite-element formulation for stress analysis under axisymmetric and non-axisymmetric conditions. Their axisymmetric analysis explored the free and constrained inflation of a flat circular membrane, the latter with respect to inflation against different geometries including a circular cylindrical surface, a 60° conical surface, and a horizontal plate. For the non-axisymmetric experiment, they investigated the free and constrained inflation of an elliptical membrane with uniform properties. They were the first to include developing contact boundary conditions in their hyperelastic finite-element formulation and used the single-parameter Neo-Hookian energy density model to approximate the constitutive behavior. For validation purposes, they compared the experimentally measured deformation profiles and principal stretches with the finite-element predictions and were able to show reasonable agreement.

Despite the extensive research on inflation of hyperelastic (rubber-like) materials in the literature, most of the studies used uniform geometries or uniform material distributions. Also, most of the problems investigated were limited to axisymmetric geometries, with only rare attention paid to non-axisymmetric inflation. In this study, the inflation of circular rubber membranes with nonuniform thicknesss and material properties is investigated. While a membrane with uniform material properties and constant thickness can only achieve a certain deformed configuration upon pressurization, changing the distribution of stiffness and thickness over the membrane surface can result in a wider range of axisymmetric and non-axisymmetric configurations. Here, an experimental study is performed to explore the mechanics of several inflated circular membranes of uniform and heterogeneous thickness and material property distributions. Large deformation, hyperelastic finite-element simulations are validated to the experimental results, and additional simulations are performed to study parameter sensitivities and other possible inflation shapes.

This chapter proceeds as follows. Section 3.2 presents how the membrane specimens are

made and how the rubber material is mechanically characterized. Section 3.3 describes the experimental inflation setup and the data collection. Section 3.4 presents the experimental results of the inflation of axisymmetric membranes with different thickness distributions, This is followed by associated numerical results and a parameter study of potential instabilities. Section 3.5 presents the inflation results of non-axisymmetric membranes having either nonuniform thickness or nonuniform materials properties. Summary and conclusions are provided in Section 3.6.

3.2 Material characterization

Multiple tests were performed to mechanically characterize and fit the constitutive behavior of available silicone rubber materials with an appropriate hyperelastic strain energy density function assuming isotropy and incompressibility. These constitutive tests include (1) uniaxial tension, (2) planar tension, and (3) equi-biaxial tension. Although other loading conditions (such as simple compression and volumetric compression) could also be investigated, these three experiments are sufficient to encompass the stress states experienced during membrane inflation. To determine the parameter values of the strain energy density function, a nonlinear least squares optimization is used to simultaneously fit the three types of constitutive data. For each constitutive test, multiple samples were tested and a representative sample from each set was chosen for fitting.

3.2.1 Specimen synthesis and preparation

The specimens for the constitutive tests were made by mixing two-parts silicone rubber (EcoFlex 00-30, DragonSkin 20, and DragonSkin 30, obtained from Smooth-On, Inc.) in equal mass amounts and casting them into the corresponding mold for each test. A 1% weight-ratio white pigment was added to the mixture to produce a uniform white color to improve contrast during optical imaging. The liquid mixture was then allowed to cure in the mold at room temperature for several hours. After curing, a thin wax paper stencil that had been laser cut with an appropriate grid for markers, was placed on top of each specimen. A small amount of the same liquid rubber mixture was again prepared, this time with a 10% weight-ratio black pigment added to the mixture. The black mixture was then sprayed across the stencil and allowed to cure for a few hours. Finally, the wax paper was removed from the sample, leaving black imprints of the grid behind.

The black dots on the specimens were used to measure the deformation of the specimens over time using 3D photogrammetry. For this purpose, a camera was placed in front of the uniaxial and planar tension specimens and high contrast images were taken at a fixed

frequency during the constitutive tests. The change in the distance between the black dots was used to measure strains and stretches in different directions. Equi-biaxial data was collected by 3D tracking of black dots during the inflation of a uniform circular membrane, as the state of stress is equi-biaxial in the vicinity of the crown (center) of the membrane. For this purpose (and for all the subsequent membrane experiments), a setup with nine cameras tracked the 3D position of black dots on the surface of the membrane at fixed time intervals. After calibrating the cameras, the 3D coordinates of each black dot was obtained using the PhotoModeler software ([95]) at each time instant.

3.2.2 Constitutive tests

Uniaxial tension: Uniaxial tension samples were made according to the ASTM D412-26 standard. As shown in Figure 3.1A, the uniaxial tension specimen is a dog-bone shaped specimen that was cast in a mold to produce a relatively long gage section of $L_0 = 33$ mm, width of $w_0 = 13$ mm, and uniform thickness of $h_0 = 6.4$ mm. Despite knowing the depth of the mold, the thickness of each specimen was measured by a micrometer before each tested. Figure 3.1B shows a typical uniaxial tension specimen installed in pneumatic grips within an axial load-frame before the test.

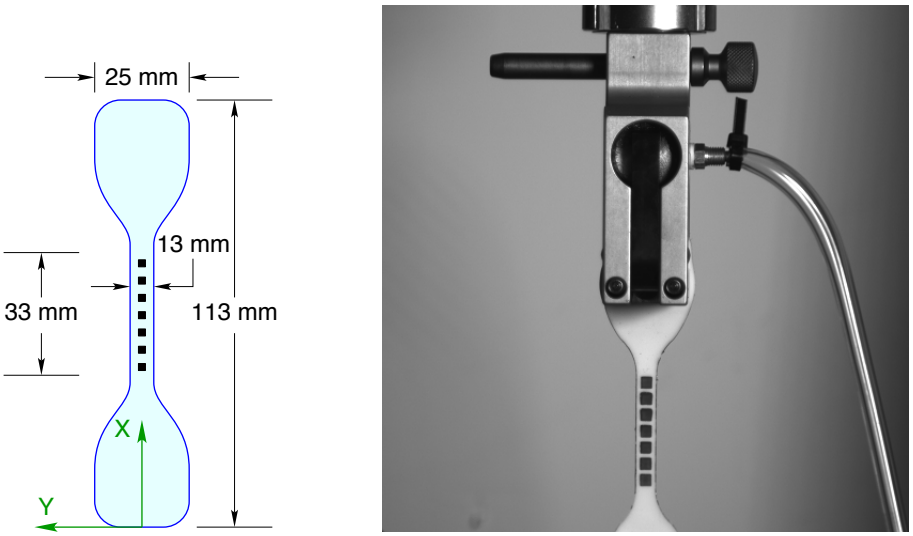

A. schematic B. photograph of specimen within grips

Figure 3.1: Uniaxial tension specimen.

Consistent with the mechanical response of soft monolithic elastomers, the rubber material is assumed to be incompressible and the deformation is isochoric (volume preserving). The uniaxial tension (pure tension) state is described by the deformation gradient ($\boldsymbol{F}$) and

Cauchy stress ($\boldsymbol{\sigma}$) tensors

$$\boldsymbol{F}_{\text{uniax}} = \begin{bmatrix} \lambda & 0 & 0 \\ 0 & \lambda^{-1/2} & 0 \\ 0 & 0 & \lambda^{-1/2} \end{bmatrix}, \quad \boldsymbol{\sigma}_{\text{uniax}} = \begin{bmatrix} \sigma & 0 & 0 \\ 0 & 0 & 0 \\ 0 & 0 & 0 \end{bmatrix}, \tag{3.1}$$

where the principal stretches are $\lambda_1 = \lambda$ (along the tension axis) and $\lambda_2 = \lambda_3 = \lambda^{-1/2}$ (lateral and out-of-plane). In addition, for an isotropic incompressible material, the axial Cauchy stress $\sigma_1 = \sigma$ can be calculated by differentiating the strain energy density function $W(I_1, I_2)$ with respect to the I_1 and I_2 invariants of the left Cauchy-Green deformation tensor ($\boldsymbol{B} = \boldsymbol{F}\boldsymbol{F}^\top$) according to

$$\boldsymbol{\sigma} = -q\boldsymbol{I} + 2\left[\frac{\partial W}{\partial I_1}\boldsymbol{B} - \frac{\partial W}{\partial I_2}\boldsymbol{B}^{-1}\right], \tag{3.2}$$

where q is a scalar field that enforces the incompressibility constraint. Under plane stress conditions, q is found by setting the out-of-plane principal stress $\sigma_3 = 0$. The first two principal invariants of $\boldsymbol{B}$ are defined as

$$I_1 = \lambda_1^2 + \lambda_2^2 + \lambda_3^2, \quad I_2 = \lambda_1\lambda_2 + \lambda_2\lambda_3 + \lambda_3\lambda_1, \tag{3.3}$$

where λ_1, λ_2, and λ_3 are the principal stretch ratios. The third principal invariant of $\boldsymbol{B}$ is $I_3 = \lambda_1^2\lambda_2^2\lambda_3^2$, which is equal to unity here since the deformation is isochoric ($\lambda_1\lambda_2\lambda_3 = 1$). Equating the uniaxial stress state of Equation (3.1) to the Cauchy stress tensor of Equation (3.2), the unknown hydrostatic pressure q and axial stress σ can be obtained.

Planar tension: Since the deformation at the clamped edge of a membrane during inflation is pure shear with $\lambda_2 = 1$, the planar tension test is intended to provide a similar loading state. The planar tension specimen, as shown in Figure 3.2, is a wide rectangular sample subjected to vertical tension across a short gage length. The specimen, when installed in the grips, has a $L_0 = 25$ mm gauge length, $w_0 = 200$ mm width, and thickness of $h_0 = 2.5$ mm. The thickness of each specimen was measured after the sample was cured to account for any possible inconsistency in casting. The objective is to constrain the lateral (width) direction such that all specimen thinning occurs in the thickness direction. As shown in Figure 3.2B, the planar tension specimen is gripped along its longer (horizonal) edges to constrain the width stretch ratio ($\lambda_2 = 1$) while stretching the short (vertical) dimension ($\lambda_1 = \lambda > 1$). During testing, the specimen draws inward somewhat at the left and right right edges, so the markers were used to confirm that most of the width (away from the free edges) maintained its initial dimensions.

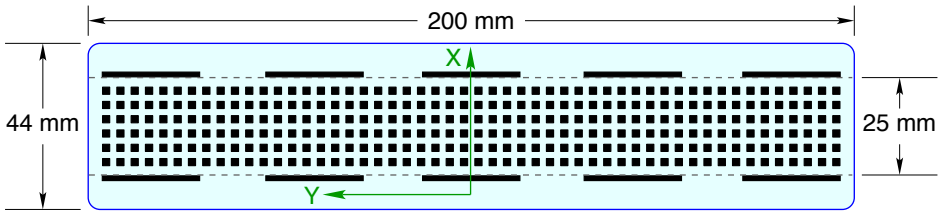

A. schematic

B. photograph of specimen in load-frame

Figure 3.2: Planar tension specimen.

Similar to the formulation for a pure tension stress and strain state, the planar tension state of an isotropic incompressible nonlinear elastic material is

$$\boldsymbol{F}_{\text{planar}} = \begin{bmatrix} \lambda & 0 & 0 \\ 0 & 1 & 0 \\ 0 & 0 & \lambda^{-1} \end{bmatrix}, \quad \boldsymbol{\sigma}_{\text{planar}} = \begin{bmatrix} \sigma & 0 & 0 \\ 0 & \sigma_2 & 0 \\ 0 & 0 & 0 \end{bmatrix}. \tag{3.4}$$

Accordingly, the unknown hydrostatic pressure q and in-plane principal stresses $\sigma_1 = \sigma$ and σ_2 can be calculated by equating the planar tension stress state of Equation (3.4) to the Cauchy stress tensor of Equation (3.2).

Equi-biaxial tension: The equi-biaxial test data is often obtained using a biaxial load-frame simultaneously stretching a thin cruciform specimen in two perpendicular directions. Here, however, we opted to measure the pressure and the deformation near the crown of an inflated uniform circular membrane for that purpose. At the vicinity of the crown, the two principal curvatures and stretches of the inflated membrane are equal ($\lambda_1 = \lambda_2 = \lambda$) and the stress state of an isotropic membrane is equi-biaxial ($\sigma_1 = \sigma_2 = \sigma$). A flat circular specimen with uniform geometry and material was prepared (Figure 3.3). The specimen was

cast in an aluminum mold with an overall diameter of $D = 178$ mm (7 in) and depth of $h_0 = 3.2$ mm (0.125 in), as shown in Figure 3.3A. Once clamped in the inflation setup, the effective diameter of the membrane is $D_0 = 152$ mm (6 in).

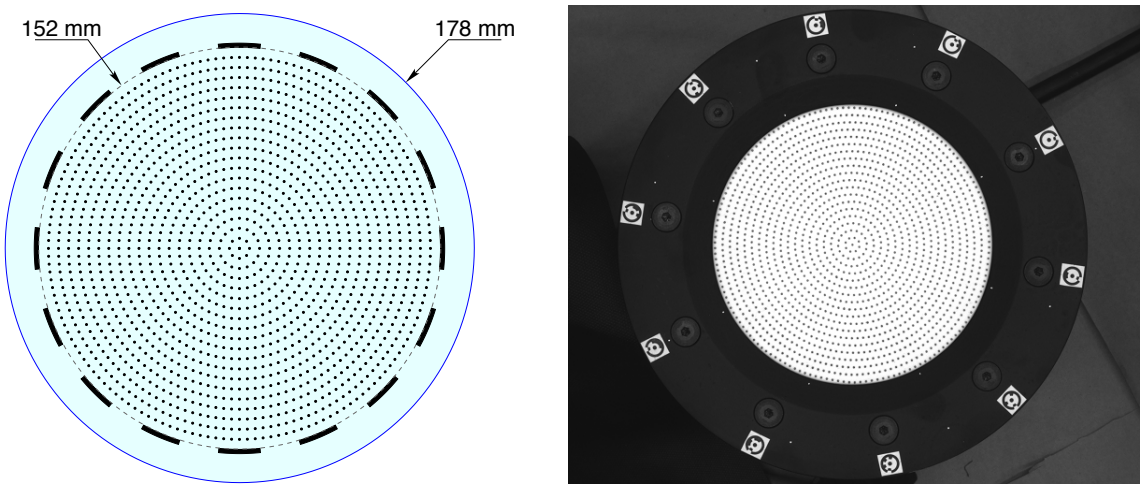

A. schematic B. photograph of installed specimen

Figure 3.3: Membrane inflation specimen used to obtain equi-biaxial tension (crown) data.

For this experiment, the deformation gradient and the stress tensor at the crown are

$$\boldsymbol{F}_{\text{biax}} = \begin{bmatrix} \lambda & 0 & 0 \\ 0 & \lambda & 0 \\ 0 & 0 & \lambda^{-2} \end{bmatrix}, \quad \boldsymbol{\sigma}_{\text{biax}} = \begin{bmatrix} \sigma & 0 & 0 \\ 0 & \sigma & 0 \\ 0 & 0 & 0 \end{bmatrix} \tag{3.5}$$

Similarly, the equi-biaxial stress σ can be obtained from equations Equation (3.2) and Equation (3.5).

3.2.3 Hyperelastic strain energy models

To model the constitutive behavior of the rubber material, we considered several hyperelastic strain energy density functions (W), including the Mooney-Rivlin, Gent, Gent-Mooney, Gent-Gent, Yeoh, and Ogden models. (Other models, such as Neo-Hooken and Arruda-Boyce which have no I_2 dependence, were not included, since our materials exhibited a dependence on I_2.) These models were simultaneously fitted to the measured stress-stretch data of the three constitutive tests. These hyperelastic models differ in their range of applicability, the number of parameters, and their ability to predict the constitutive response of real rubber materials. The energy density function of each model along with their parameters and the

corresponding small-strain shear modulus (μ_0) of each model are summarized and tabulated in Table 3.1.

Table 3.1: The hyperelastic strain energy density models considered.

Model	W	Parameters	μ_0
Mooney-Rivlin	$c_1(I_1-3)+c_2(I_2-3)$	$c_1,\ c_2$	$2\,(c_1+c_2)$
Gent	$-c_1 J_\mathrm{m}\ln\left(1-\frac{I_1-3}{J_\mathrm{m}}\right)$	$c_1,\ J_\mathrm{m}$	$2c_1$
Gent-Mooney	$-c_1 J_\mathrm{m}\ln\left(1-\frac{I_1-3}{J_\mathrm{m}}\right)+c_2\,(I_2-3)$	$c_1,\ J_\mathrm{m},\ c_2$	$2\,(c_1+c_2)$
Gent-Gent	$-c_1 J_\mathrm{m}\ln\left(1-\frac{I_1-3}{J_\mathrm{m}}\right)+3c_2\ln\left(\frac{I_2}{3}\right)$	$c_1,\ J_\mathrm{m},\ c_2$	$\frac{2}{3}\,(3c_1+c_2)$
Yeoh	$\sum_{i=1}^{3} c_i(I_1-3)^i$	$c_1,\ c_2,\ c_3$	$2c_1$
Ogden	$\sum_{i=1}^{3}\frac{\mu_i}{\alpha_i}(\lambda_1^{\alpha_i}+\lambda_2^{\alpha_i}+\lambda_3^{\alpha_i}-3)$	$\mu_1,\ \mu_2\ ,\ \mu_3,$	
		$\alpha_1,\ \alpha_2,\ \alpha_3$	$\frac{1}{2}\sum_{i=1}^{3}\alpha_i\mu_i$

Since in this study the experimental measurements will be interpreted with respect to their reference (initial) dimensions, the Cauchy stress (σ) of Equation (3.2) must be divided by the amount of stretch in its corresponding direction (λ) to obtain the engineering (first Piola-Kirchhoff) stress $\sigma_\mathrm{eng}=\sigma/\lambda$. The results of simultaneous curve fitting to experimental data of the Smooth-On's EcoFlex 00-30 silicone rubber, the most prevalent rubber material in this research, is presented in Figure 3.4 for each strain energy model. The best fit was obtained with the Ogden model, with the Gent-Mooney and Gent-Gent models being next best, for stretches in the range $1\leq\lambda<3$. Table 3.2 summarizes the value of coefficients obtained for each energy density function.

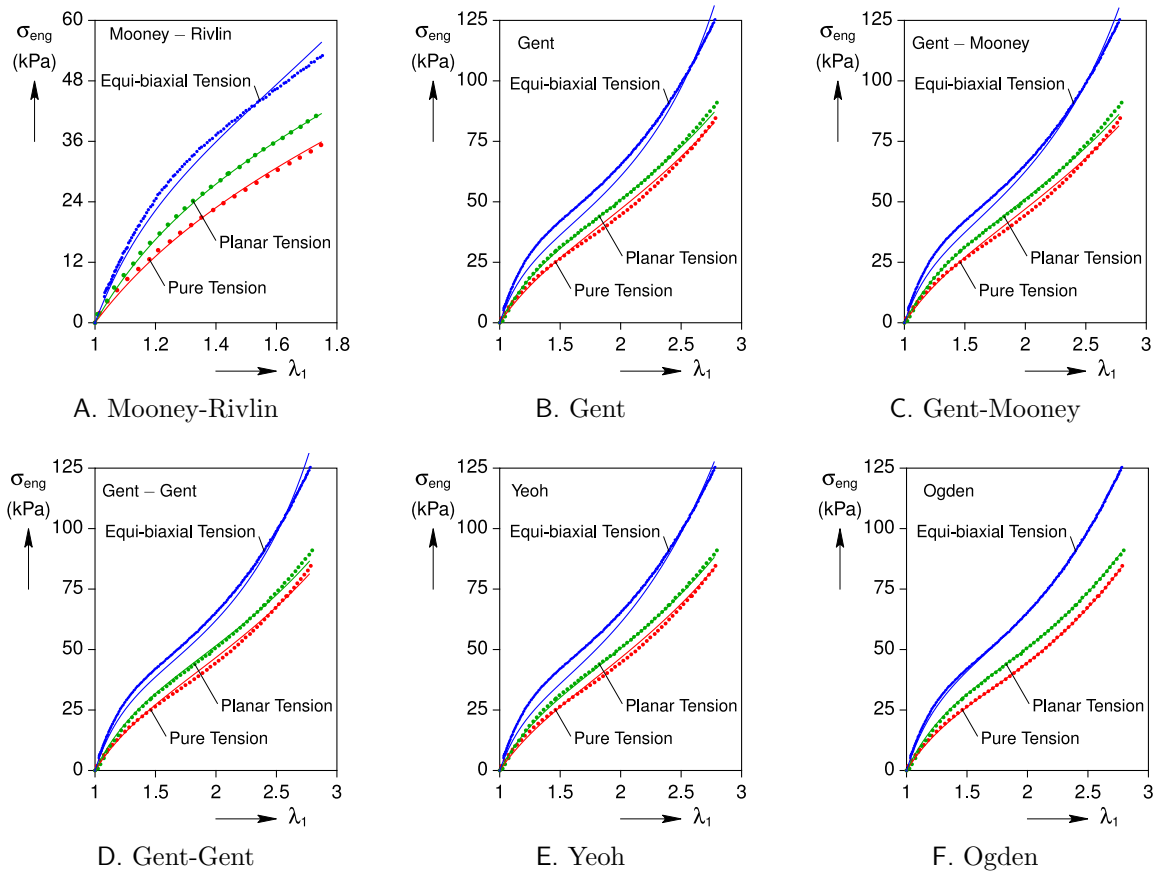

Figure 3.4: Simultaneous fitting of different hyperelastic models to the experimentally measured data for EcoFlex 00-30. The constitutive tests include pure, planar, and equi-biaxial tension. Experimental data (dots) and hyperelastic model fit (solid lines).

Table 3.2: Coefficient values of each energy density model, obtained from simultaneous fitting to the experimental data of EcoFlex 00-30.

Model	**Coefficients**	$\boldsymbol{\mu_0}$ (kPa)
Mooney-Rivlin	c_1 =11.73 kPa, c_2 =1.55 kPa	26.56
Gent	c_1 =12.39 kPa, J_{m} =26.05	24.78
Gent-Mooney	c_1 =12.41 kPa, J_{m} =28.50, c_2 =0.20 kPa	25.21
Gent-Gent	c_1 =11.90 kPa, J_{m} =25.27, c_2 =3.64 kPa	26.22
Yeoh	c_1 =12.13 kPa, c_2 =0.26 kPa, c_3 =0.01 kPa	24.26
Ogden	μ_1 =50.42 kPa, μ_2 =1.41 kPa, $\mu_3 = -0.82$ kPa, α_1 =0.89, α_2 =4.48, $\alpha_3 = -2.32$	26.53

3.3 Inflation apparatus and data collection

The membrane inflation setup, shown in Figure 3.5, is an experimental apparatus custom-built for the purpose of the membrane inflation experiments in this research. The setup is designed to use pressurized air for inflation. (It could be modified to use liquids, e.g. glycerin, as well). The effective diameter of the inflation chamber is 152.4 mm (6 in) to accommodate "hand-size" membranes.

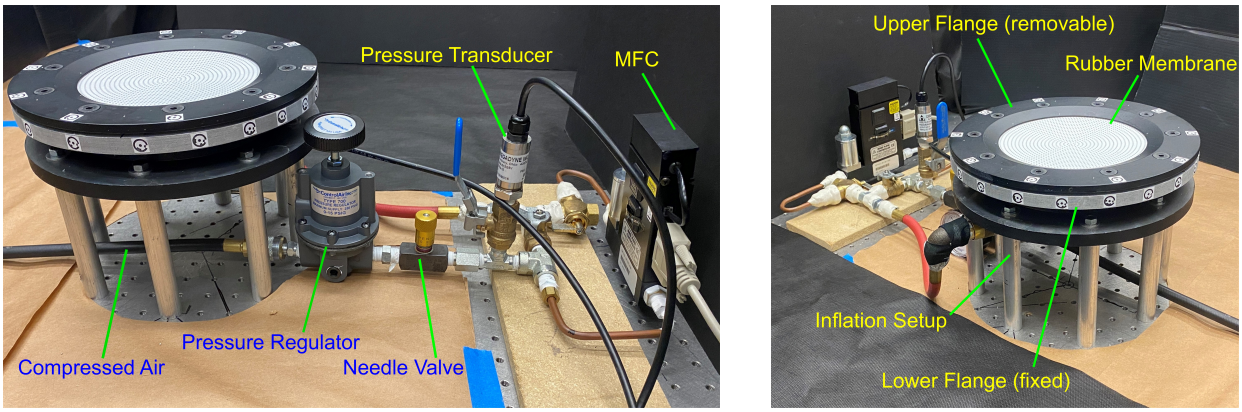

A. View 1 B. View 2

Figure 3.5: Experimental setup for circular membrane inflation.

Compressed shop air (approximately 100 psi pressure) initially enters a circuit of tubing before being delivered to the inflation chamber. As shown in Figure 3.5A, the compressed air is first regulated using a pressure regulator at the upstream of the circuit. It then passes through a fine-adjust needle valve to enter a mass flow controller (MFC) that can be set to provide a specific flow rate of gas (air here) to the inflation chamber. In this setup, the MFC (AAlborg GFC 17) can be set to provide a volume flow rate between 0-200 cubic centimeter per minute (ccm) which can be either specified locally on the device or remotely set using a data acquisition (DAQ) system. A pressure transducer (Omega PX309-015AV) is placed in line with the circuit, just before the MFC inlet to measure and monitor the upstream pressure. The air coming out of the MFC is than passed through an air-hose to the bottom of the inflation chamber. The inflation chamber is equipped at the bottom with a second pressure transducer (Omega PX309-005AV) to measure the pressure underneath the inflated membrane.

A National Instruments (NI) 16-Bit USB-6251 DAQ (16 analog inputs at 1.25 MS/s, 2 analog outputs at 2.86 MS/s) is used to collect the pressure data from the two pressure transducers and volume flow rate data from the MFC. The DAQ also sets the desired value of the MFC volume flow rate and triggers the nine cameras for synchronized imaging. All

data collection and device control commands are performed in NI LabView software through a custom-written program.

Through the use of multiple CCD cameras (nine here), digital photos are taken simultaneously at constant time increments during each experiment. All cameras, although having different CCDs, are 5 Megapixel machine-vision monochromes with 25 mm wide-angle lenses, and the cameras are triggered by the DAQ system to obtain synchronized sets of images during the inflation process. Prior to the experiments, each camera is calibrated using multiple photos of a calibration grid (Figure 3.6) at different orientations. The photogrammetry technique is utilized to measure the non-uniform deformation of the inflated membrane by tracking the black dots on its surface. PhotoModeler software (Version 2020.2.1) is used to obtain the 3D locations of each black dot on the membrane by ray tracing, and each dot must be in the view of at least three cameras (hence the need for so many).

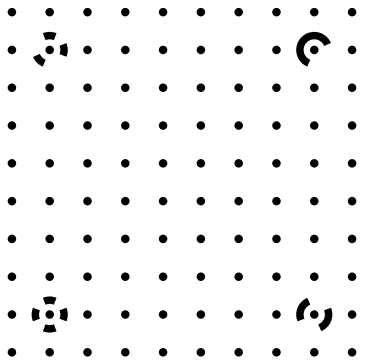

Figure 3.6: PhotoModeler grid used to calibrate the cameras.

As shown in Figure 3.7A, every membrane was painted with nearly equally spaced black dots in a polar grid. After a small amount of radial pre-stretch is applied, the membrane is clamped in the inflation setup using 10 capscrews. The X-Y plane of the cartesian coordinates coincides with the top surface of the undeformed membrane and Z is the normal (vertical) direction. (Since the membranes are thin relative to their radius, the usual kinematic assumption in membrane theory of using the midsurface is only a minor discrepancy.) Moreover, since the reference membrane is circular, it is also convenient to use a cylindrical frame with (R, Θ, Z) coordinates, where $X = R\cos\Theta$, $Y = R\sin\Theta$, and $Z = Z$. In this way, $\Theta = 0^\circ$ and $\Theta = 90^\circ$ correspond to the positive X and positive Y directions, respectively. Corresponding current coordinates are denoted by lower case variables (x, y, z) and (r, θ, z) in the respective cartesian and cylindrical frames.

Using the photogrammetry data, the typical initial distribution of the black dots is measured (Figure 3.7B). In this schematic the black dots are shown as red, green, and blue nodes for illustration purposes, and a Delauney grid with triangular elements is constructed

to connect these nodes. The grid serves as a finite-element mesh to reconstruct the 3D surface deformation of the membrane. Although perhaps not obvious in the photograph (Figure 3.7A), the installed membrane sags downward slightly, due to the the self weight of the membrane and the small inward radial extrusion during clamping. The upper flange of the inflation fixture also has an array of stationary markers that are used to define the coordinate frame during membrane inflation. For each experiment, the 3D history of black dots on the membrane are post-processed using a self-developed Mathematica code, and the results are presented in terms of deformation profiles, stretch ratios, and invariants of the left Cauchy-Green deformation tensor.

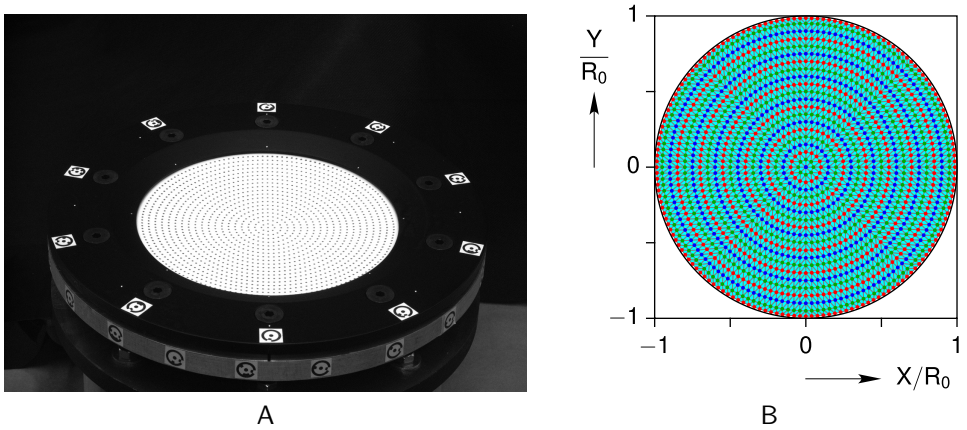

Figure 3.7: Array of black dots on the circular membrane. (A) Photograph of the painted membrane in the setup before inflation begins and (B) a plan view of the 2D polar grid of the dots measured by photogrammetry.

3.4 Axisymmetric membrane inflation

This section presents the experimental and numerical results of the inflation of initially flat circular rubber membranes with axisymmetric thickness distributions. Three different membrane thickness distributions are studied and compared, including a uniform thickness (distribution D0), radially increasing thickness (distribution D1), and radially decreasing thickness (distribution 2). For these axisymmetric membranes, the thickness varies linearly from the center towards the outer radius (R_0) as

$$h(R) = h_0 \left[(\eta - 1) \frac{R}{R_0} + 1 \right], \tag{3.6}$$

where R is the reference radial coordinate, $\eta = h_1/h_0$, is the normalized slope, h_0 is the thickness of the membrane center, and h_1 is the thickness at the clamped edge. Moreover,

it is required that $h(R) > 0$. Distribution D0 has $\eta = 1$, distribution D1 has $\eta > 1$, and distribution 2 has $0 < \eta < 1$. The material used in all three cases is Ecoflex 00-30 (EF30) silicone rubber.

The uniform thickness (and material) circular membrane has been extensively studied (mostly numerically) in literature, and is used as a baseline for material characterization and validation of the finite-element analysis (FEA). The experimentally measured data for each thickness distribution is first presented, followed by a numerical finite-element study that compares the experimental measurements to FEA predictions. Subsequently, a parametric study on the effect of thickness distributions on the deformation and instability of axisymmetric circular rubber membranes is presented.

3.4.1 Distribution D0 (uniform thickness)

Experimental results for the uniform thickness membrane (Figure 3.8A) are presented below. The initial average thickness is about 2.97 mm (0.117 in), measured by a micrometer at multiple locations across the membrane. Figures 3.8C–3.8F show snapshots from one of the nine cameras at four time instants during inflation.

The pressure p and volume V (the change in the enclosed volume by the membrane) histories during inflation are provided in Figures 3.9A and 3.9B. The volume history can be obtained in two ways: (1) measure the volume by time integration of the output of the MFC, and (2) use the 3D deformed surface of the membrane, constructed by delauney triangulation of the black dot locations, to calculate the enclosed volume. This is obtained by summing the signed projected area (on the $Z = 0$ plane) of each triangular element multiplied by its centroidal height. As shown in Figure 3.9A, the two approaches yield the same result. It should be mentioned, however, that the second approach is only feasible when all (or most) of the black dots are tracked successfully (are in view of at least three cameras) during inflation, such that the deformed surface of the membrane can be approximated to acceptable accuracy. The pressure-volume cross plot is shown in Figure 3.9C, which exhibits the sigmoid-like trajectory typical of inflated membranes. It is observed that after an early small nonlinear segment, the pressure-volume response follows a straight line up to about $p = 2$ kPa. After $p = 2$ kPa, the pressure-volume response reaches a 'knee' and the slope decreases to a smaller value where a small increase in p is accompanied by a large increase in V.

Figure 3.10 provides information about the membrane's response near the crown ($R = 0$), in terms of the equi-biaxial stretch ratio λ_0, curvature κ_0 and Cauchy stress σ_0. In particular, the pressure-crown stretch data is shown in Figure 3.10A. The membrane starts from a nearly undeformed state ($\lambda_R = \lambda_\Theta = \lambda_0 \approx 1$) and the crown reaches a stretch ratio of

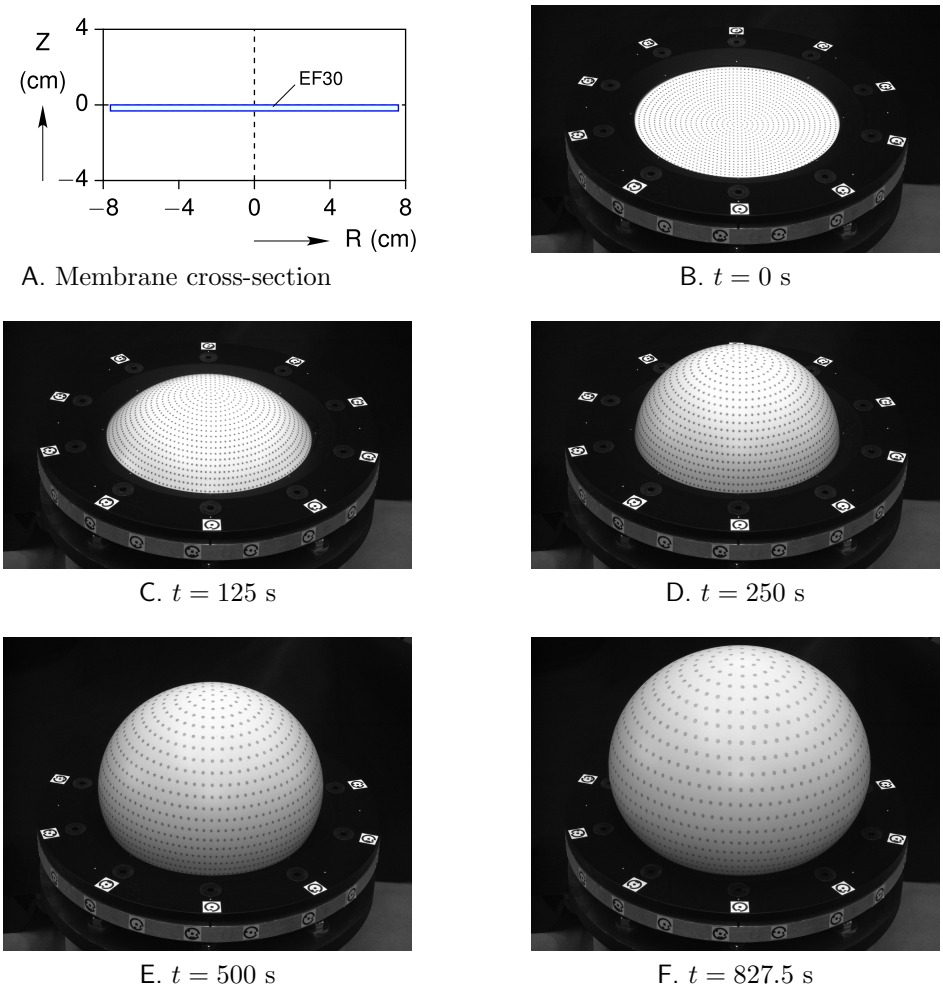

A. Membrane cross-section

B. $t = 0$ s

C. $t = 125$ s

D. $t = 250$ s

E. $t = 500$ s

F. $t = 827.5$ s

Figure 3.8: Photographs of the uniform membrane (distribution D0) at selected times during inflation.

about $\lambda_0 = 2.9$ at $p = 2.7$ kPa. (Note, while a bit unconventional, the subscripts R and Θ refer to the reference coordinates rather than the current ones, considering line elements in these reference directions as being convected to their current directions. This notation helps to make the directions unambiguous, especially later in Section 3.5 when considering non-axisymmetric membrane inflations.) Due to axisymmetry, both principal stretch ratios, the radial stretch $\lambda_R(R)$ and the hoop stretch $\lambda_\Theta(R)$, are verified to be essentially independent of Θ throughout the membrane (only functions of R), and at the crown the two stretch ratios are equal at any time instant. The curvature of the crown (chosen positive when concave downward) with increasing pressure is provided in Figure 3.10B. The dimensionless curvature of the crown ($\kappa_0 R_0$) starts slightly negative due to the initial membrane sag, but then quickly becomes positive as inflation progresses. Interestingly, it initially increases up to about $p = 2.2$ kPa, but then reaches a maximum and decreases thereafter. Moreover,

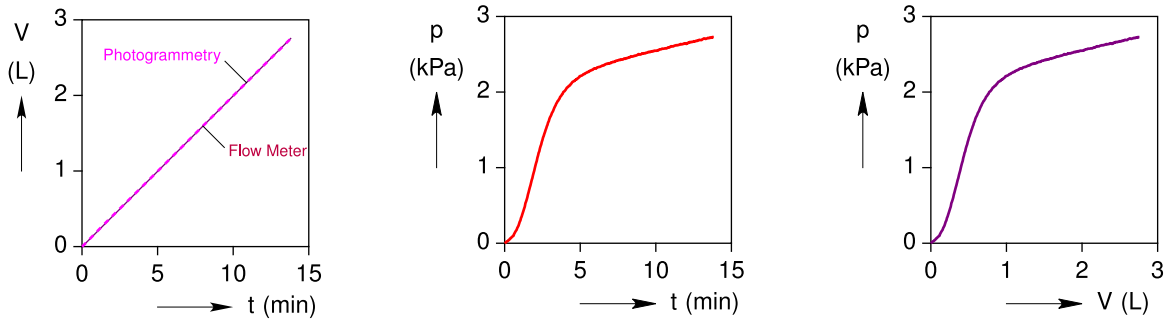

A. Volume history B. Pressure history C. Pressure-volume

Figure 3.9: Structural response of the uniform membrane (distribution D0).

because of the axisymmetry, the two principal curvatures are equal at the crown, $\kappa_R(0) = \kappa_\Theta(0) = \kappa_0$. The Cauchy stress at the crown as a function of pressure is also plotted in Figure 3.10C. At the crown, the state of stress is equi-biaxial in the two principal directions, $\sigma_R(0) = \sigma_\Theta(0) = \sigma_0$, and the stress can be readily calculated from the curvature and stretch at that point, according to

$$\sigma_0 = \frac{p}{2h\kappa_0} = \frac{p\lambda_0^2}{2h_0\kappa_0} \tag{3.7}$$

where $h = \lambda_Z h_0$ is the current thickness of the membrane at the crown and $\lambda_Z = \lambda_0^{-2}$ is the third principal stretch ratio in the through-thickness direction by the incompressibility assumption Equation (3.5). As is conventional, plane stress conditions are assumed since the membrane is thin enough that the direct stress due to the pressure (normal to the membrane surface) is negligible compared to the in-surface stresses.

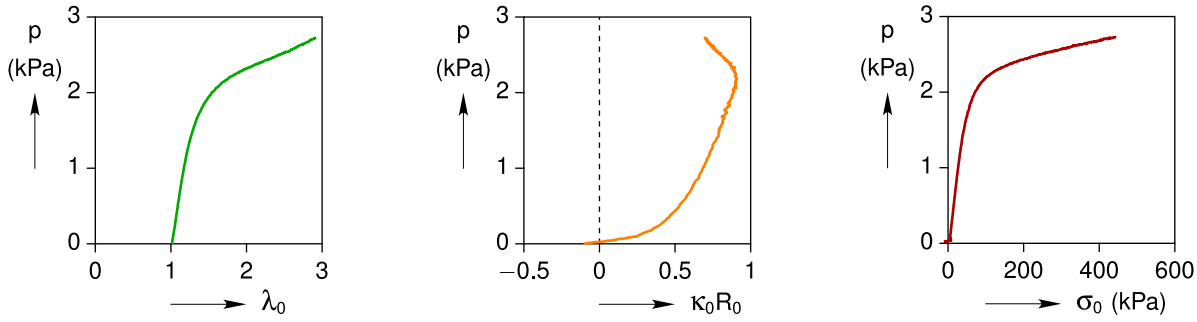

A. pressure-stretch B. pressure-curvature C. pressure-stress

Figure 3.10: Measured data at the crown of the uniform membrane (distribution D0).

The measured distribution of the two principal stretch ratios, λ_R and λ_Θ, are plotted against the dimensionless radius of the reference configuration (R/R_0) in Figure 3.11 at the

time of maximum inflation. To verify the axisymmetric deformation, the results are plotted at eight radial directions. If all the dots are tracked successfully, the values of λ_R and λ_Θ can be calculated at a maximum of 19 and 20 points, respectively, by simply calculating the ratio of current length to reference length between adjacent dots. Comparing the two principal stretch ratios, we can see that for this uniform thickness membrane, $\lambda_R > \lambda_\Theta$ at each R, except at the crown where the two are equal (Figure 3.11C). Moreover, it can be seen that the hoop stretch ratio reaches $\lambda_\Theta = 1$ at the clamped boundary, at which point $\lambda_R > 1$. This confirms that the state of deformation progresses from equi-biaxial tension at the crown (Equation (3.5)) to pure shear (Equation (3.4)) at the edge for axisymmetric inflation.

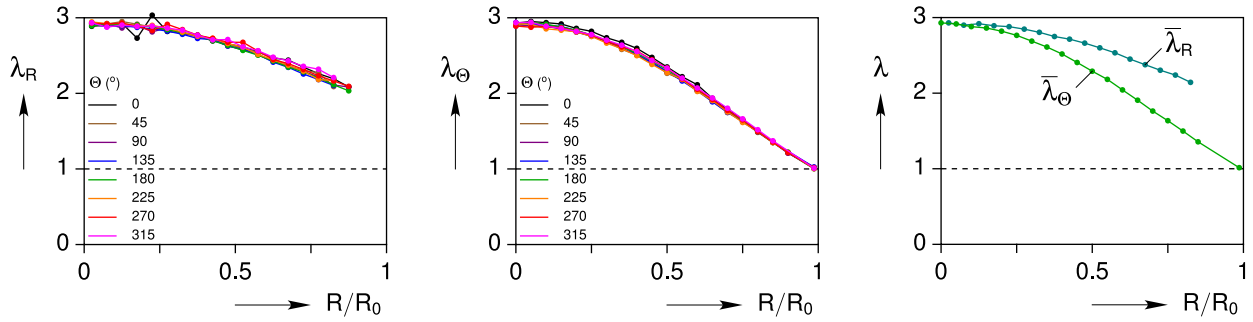

Figure 3.11: Radial distributions of the two principal stretches in the uniform membrane (distribution D0) at the time of maximum inflation.

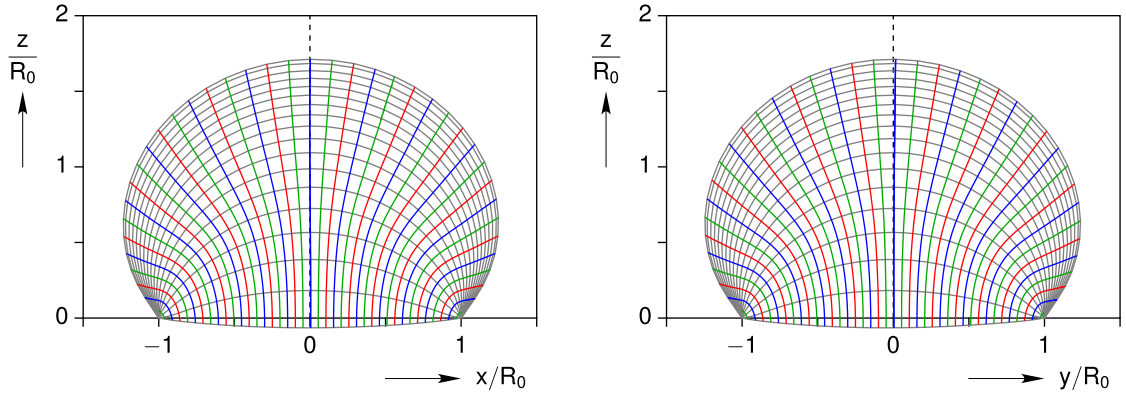

Figure 3.12: Measured deformation profiles (gray lines) and displacement histories of dots (colored lines) during inflation of the uniform membrane (distribution D0).

The dimensionless deformation profiles of the inflated membrane (gray lines) at selected times during inflation are depicted in Figures 3.12A and 3.12B on two planes ($Y = 0$ and

$X = 0$) cutting through the membrane diameter. In addition, the trajectories of the black dots during the inflation processes are provided (colored lines). It is observed that the black dot at the crown ($X = Y = 0$) displaces only vertically in the Z direction, while other dots (except at the clamp ring) displace both vertically and radially outwards.

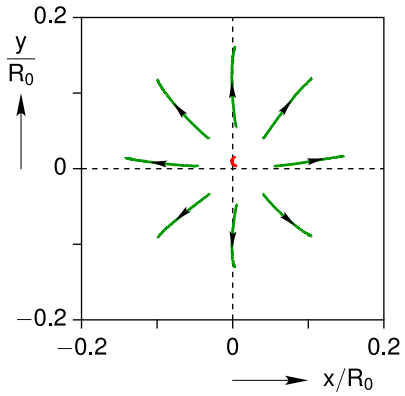

Figure 3.13: Plan view of the displacement history of the crown (red) and the eight adjacent dots (green) during inflation of the uniform membrane (distribution D0).

Viewed from above the membrane, the deformation histories of the crown and eight equally spaced dots around the crown are shown in Figure 3.13. The figure suggests that the deformation is not completely axisymmetric, as supposed to be, but it is very close to that. The deviation from axisymmetry originates from various sources, mainly due to some offset in the original placement of the membrane between the upper and lower flanges of the inflation setup, as well as inconsistencies during tightening of the bolts of the clamps. Other sources of deviation, although of secondary importance, include a slight nonuniformity in the thickness and material distributions during fabrication of the membrane.

The distributions of the left Cauchy-Green deformation tensor ($\boldsymbol{B} = \boldsymbol{F}\boldsymbol{F}^\top$) invariants across the surface of the membrane are examined next. The principal invariants in Equation (3.3), which do not depend on the rigid body motion of material elements, are often used in phenomenological hyperelastic functions, such as the Mooney-Rivlin and Gent models. Incidentally, these are the same invariants of the right Cauchy-Green deformation tensor ($\boldsymbol{C} = \boldsymbol{F}^\top\boldsymbol{F}$), as viewed in the reference configuration. Figure 3.14 provide 3D contour plots of I_1 and I_2 mapped onto the deformed configuration at the same times as in Figure 3.8. In the undeformed configuration ($\lambda_1 = \lambda_2 = \lambda_3 = 1$) the invariants are $I_1 = I_2 = 3$, so these are subtracted off the results. The quantities $I_1 - 3$ and $I_2 - 3$ correspond to two portions of the strain energy density, before they are weighted by a selected constitutive model. Overall, each time instant has a nearly axisymmetric distribution with a monotonic distribution from small values at the clamping ring to large values at the crown. The noisy patchwork-like pattern arises from the discretized mesh of constant I_1 and I_2 (constant strain) triangles used in

the post processing and the small experimental uncertainties in dot locations. Nevertheless, the results conform to expectations for a uniform inflated membrane.

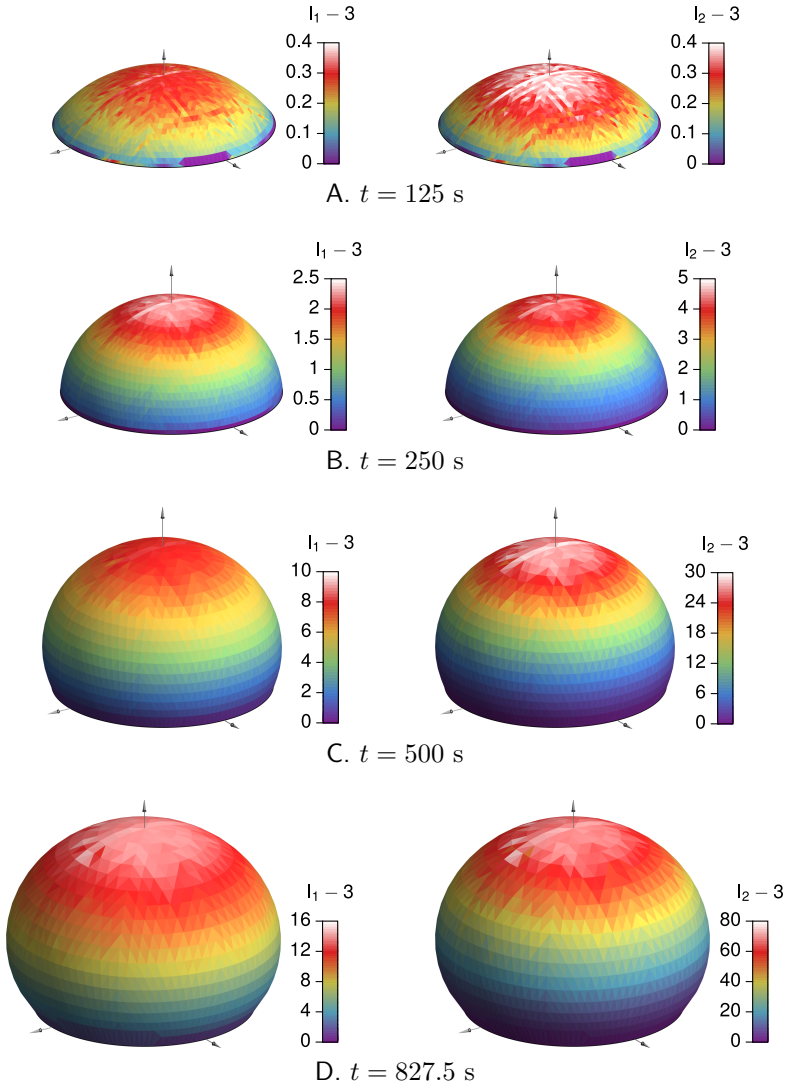

Figure 3.14: Measured contours of $I_1(\boldsymbol{B})$ and $I_2(\boldsymbol{B})$ for the uniform membrane (distribution D0).

3.4.2 Distribution D1 (radially increasing thickness)

The experimental results of the second axisymmetric case, a circular membrane with radially increasing thickness, are presented here. The membrane was fabricated using a conical mold with a negative slope (about $-4.76°$), resulting in a thickness difference of 6.35 mm (0.25 in) between the center and outer radius. Figure 3.15A shows the linear thickness distribution from 1.92 mm (0.076 in) at the center to 8.27 mm (0.326 in) at the edge, giving $\eta = 4.31$. Figures 3.15B–3.15E show snapshots of the membrane at four time

instants during inflation. In this case, the deformed shapes are more prolate (vertically oriented) than the uniform membrane in Figure 3.8.

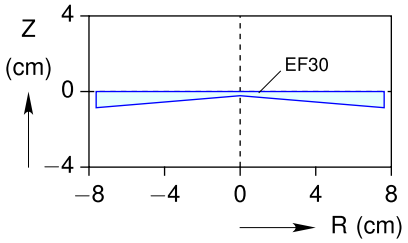

A. Membrane cross-section

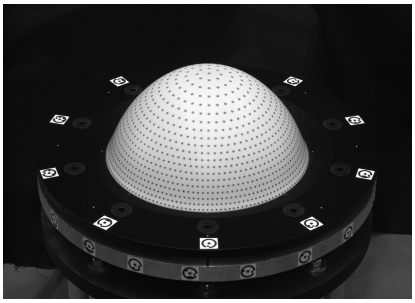

B. $t = 240$ s

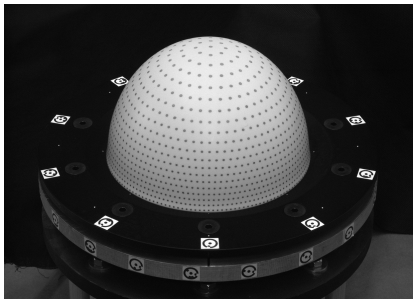

C. $t = 360$ s

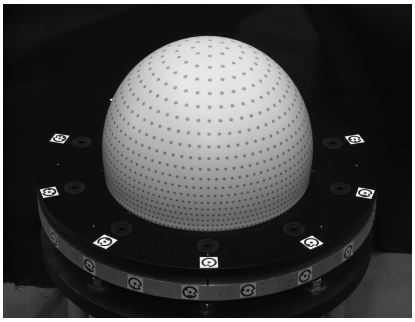

D. $t = 480$ s

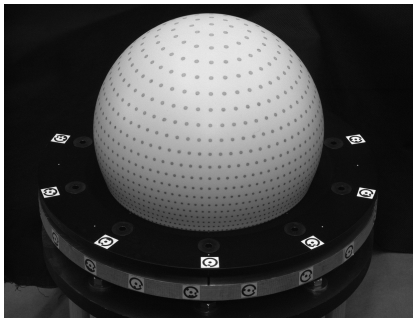

E. $t = 658$ s

Figure 3.15: Photographs of the nonuniform thickness membrane (distribution D1) at selected times during inflation.

The structural response, in terms of the inflation volume and pressure histories, are plotted in Figures 3.16A and 3.16B. The pressure-volume cross plot, shown in Figure 3.16C, exhibits an 'S-shape' response, qualitatively similar to the uniform thickness membrane (shown by the thin gray line). The pressure in this case, however, is larger, indicating a stiffer membrane overall. (The volume of rubber material in this membrane is about 2.2× that of the previous uniform thickness membrane.)

The response at the crown, shown in Figure 3.17, is qualitatively similar to the uniform membrane case but quantitatively different. The pressure-stretch data (Figure 3.17A) shows a monotonic increase of the crown stretch ratio from the undeformed state (λ_0 =1) to a

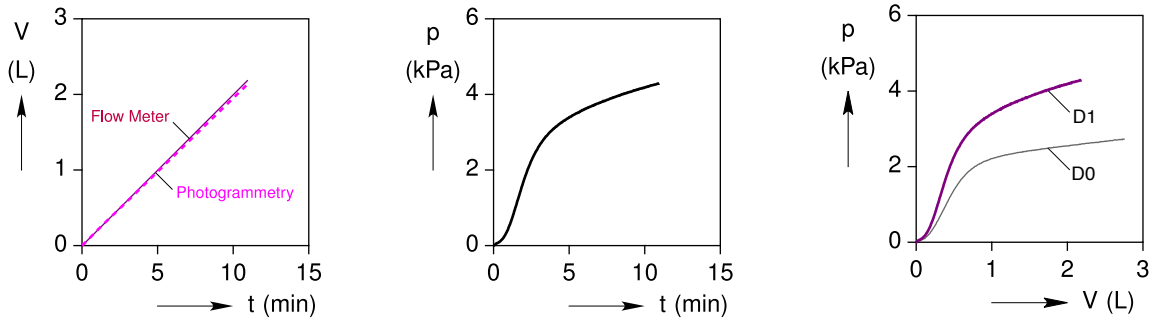

A. Volume history B. Pressure history C. Pressure-volume

Figure 3.16: Structural response of the nonuniform membrane (distribution D1).

stretch ratio of about $\lambda_0 = 3.65$ at $p = 4.3$ kPa. The evolution of crown curvature with pressure is presented in Figure 3.41B. It can be seen that the dimensionless curvature of the crown ($\kappa_0 R_0$) initially increases up to about p =3.2 kPa and then decreases thereafter. Consistent with the more prolate shape, the maximum crown curvature is larger than that for the uniform membrane. (It is unclear if the non-monotonic bump near $\kappa_0 R_0 = 0.4$ is real, since the curvature calculation is problematic with even slightly noisy position data.) The Cauchy stress at the crown as a function of pressure is shown in Figure 3.17C. The crown stress values here are much larger than those of the uniform membrane (Figure 3.10C), since the membrane center is thinner and causes a larger crown stretch ratio.

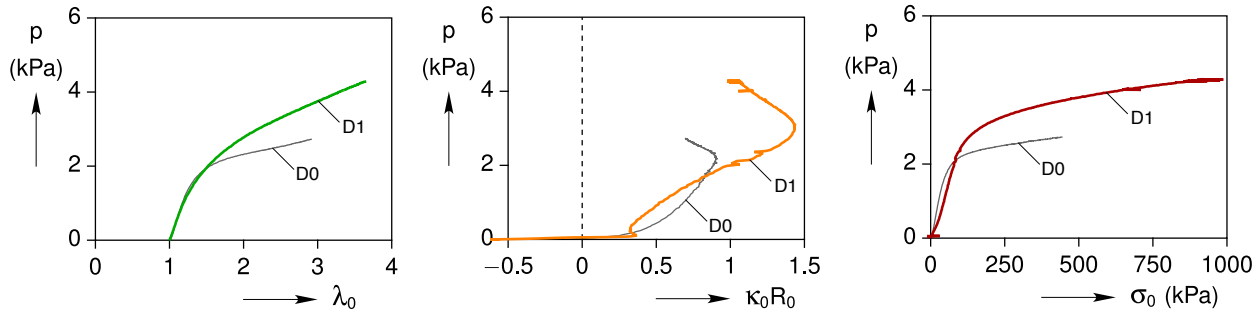

A. pressure-stretch B. pressure-curvature C. pressure-stress

Figure 3.17: Measured crown data of the nonuniform membrane (distribution D1).

The two principal stretch ratios, λ_R and λ_Θ, in the radial and hoop directions, respectively, are plotted at the time of maximum inflation as a function of R/R_0 in Figure 3.18. To verify that the inflation response is axisymmetric, the results are plotted at eight radial directions between $\Theta = 0°$ and 360°. Comparing the two principal stretch ratios, in this case $\lambda_R(R) \approx \lambda_\Theta(R)$ (Figure 3.18C), unlike the uniform membrane case where $\lambda_R(R) \geq \lambda_\Theta(R)$ (Figure 3.11C). Moreover, unlike distribution D0, λ_R decreases almost linearly in this case.

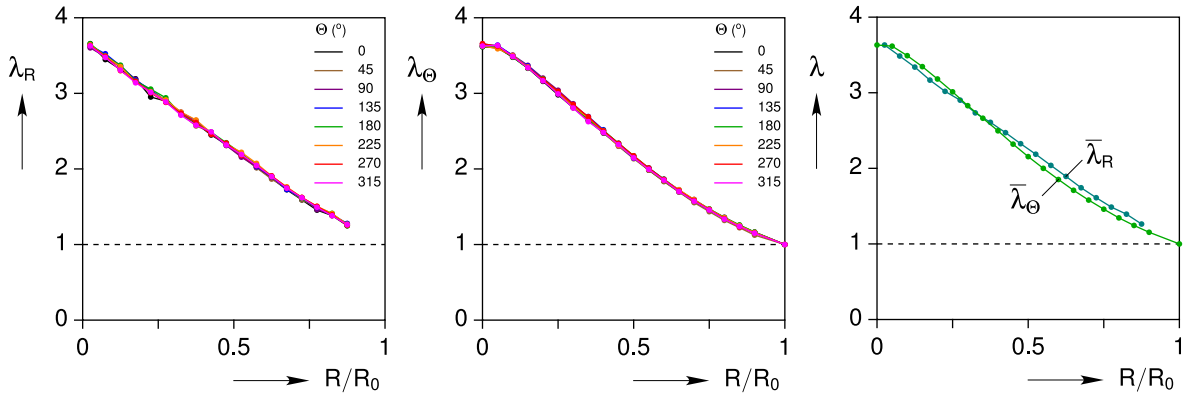

A. Radial stretch B. Hoop stretch C. Θ-averaged

Figure 3.18: Radial distributions of the two principal stretches in the nonuniform membrane (distribution D1) at the time of maximum inflation.

The dimensionless deformation profile history of the inflated membrane at selected instants of time are plotted in Figures 3.19A and 3.19B in two planes cutting through the membrane. Compared to the uniform thickness membrane, the deformation profiles bulge outward less while the vertical displacement is nearly the same. Viewed from above the membrane, the deformation histories of the crown and eight equally spaced dots around the crown are shown in Figure 3.20. The figure shows that the deformation is not perfectly axisymmetric, as it leans slightly towards the positive X direction. Nevertheless, the radial displacements are larger than in the uniform thickness case (Figure 3.13).

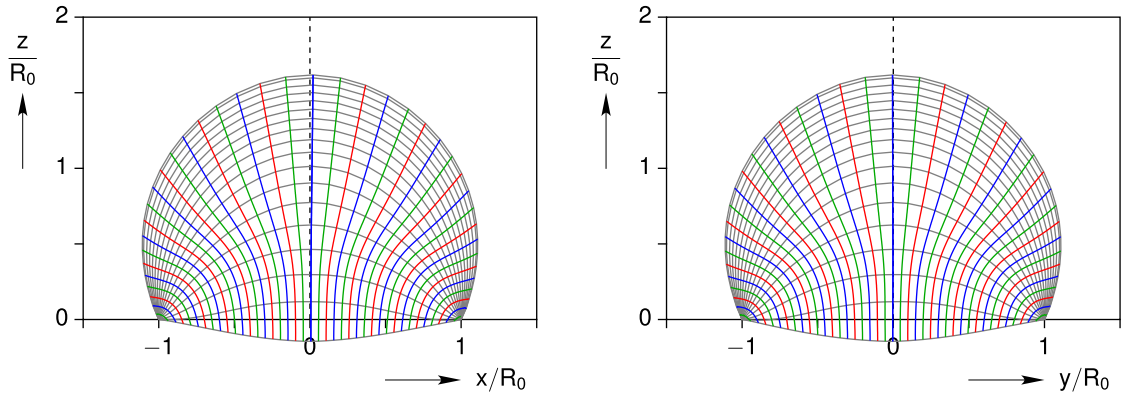

A. $Y = 0$ plane B. $X = 0$ plane

Figure 3.19: Measured deformation profiles (gray lines) and displacement histories of dots (colored lines) during inflation of the nonuniform membrane (distribution D1).

Variations of the invariants of the left Cauchy-Green deformation tensor ($\boldsymbol{B}$) across the surface of the membrane are studied next. Figure 3.21 demonstrate the 3D contour plots of the quantities $I_1 - 3$ and $I_2 - 3$ on the deformed configuration at various instants of time.

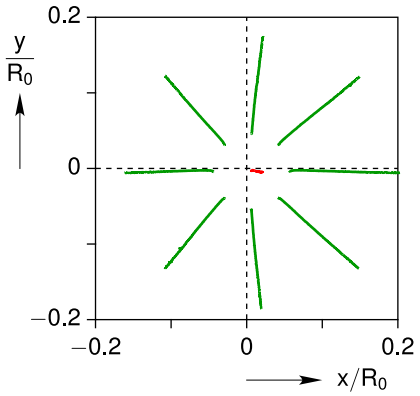

Figure 3.20: Plan view of the displacement history of the crown (red) and the eight adjacent dots (green) during inflation of the nonuniform membrane (distribution D1).

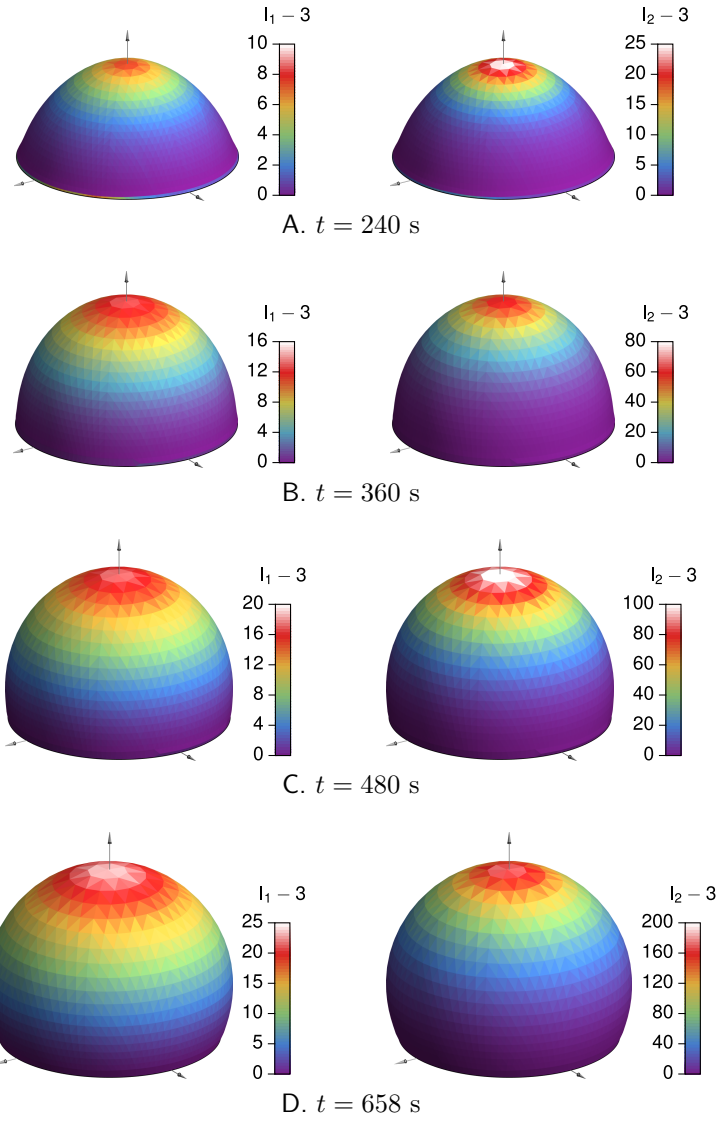

Figure 3.21: Measured contours of $I_1(\boldsymbol{B})$ and $I_2(\boldsymbol{B})$ for the nonuniform membrane (distribution D1).